Fuel Cell Drone for Soil Monitoring

Louis Cheung

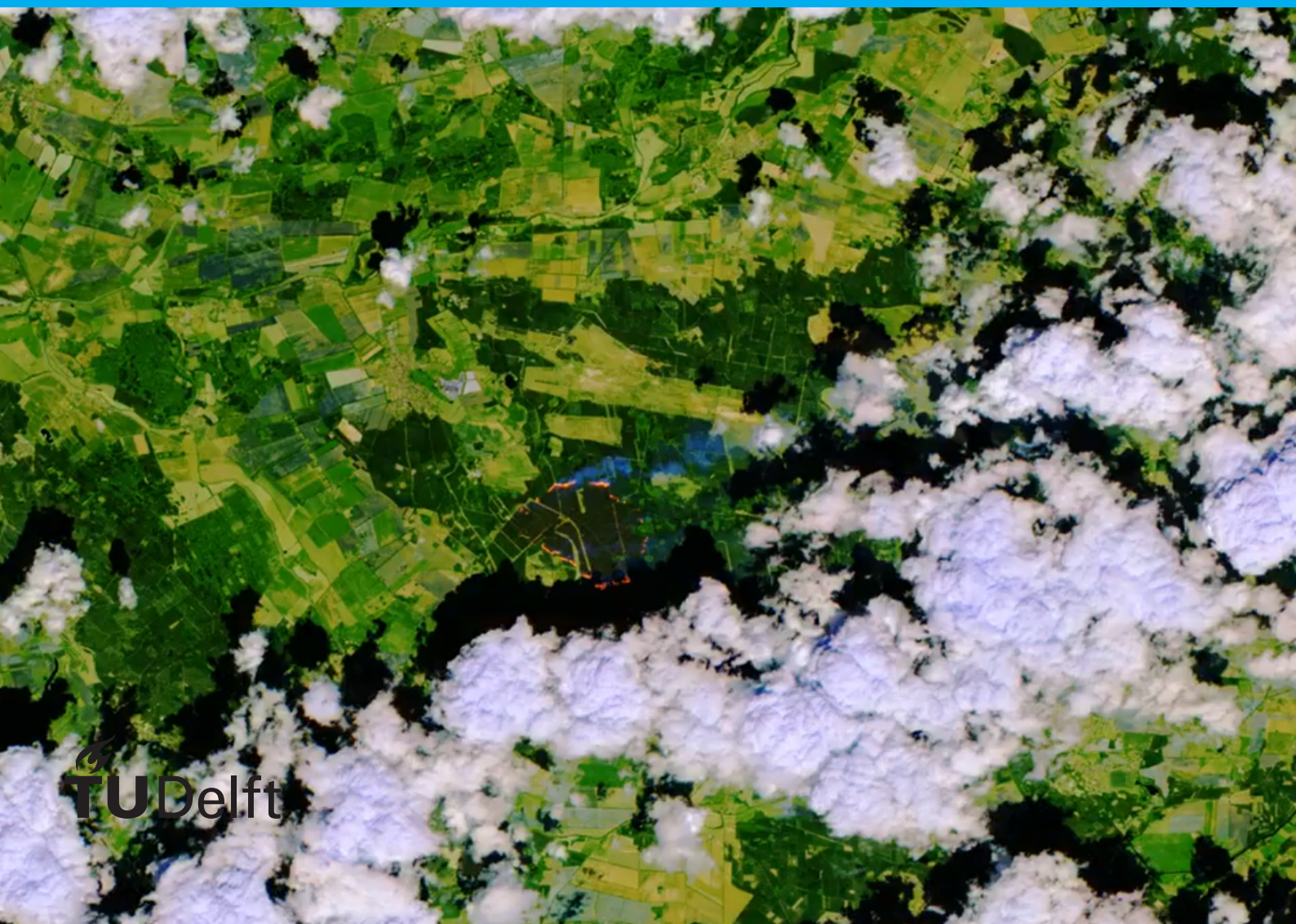

Fuel Cell Drone for Soil Monitoring

by

Louis Cheung

to obtain the degree of Master of Science
at the Delft University of Technology;
to be defended publicly on Friday May 22, 2020 at 15:00.

Student number:	4749103	
Project duration:	October 1, 2018 – June 1, 2020	
Supervisors:	Prof. dr. ir. A. Purushothaman Vellayani,	TU Delft
	Dr. Nandini Bhattacharya,	TU Delft
	Dr. Bart Remes,	TU Delft
Thesis committee:	Prof. D. Roekaerts,	TU Delft, chair
	Prof. dr. ir. A. Purushothaman Vellayani,	TU Delft
	Dr. Nandini Bhattacharya,	TU Delft
	Ir. Yash Tambi,	TU Delft

An electronic version of this thesis is available at `http://repository.tudelft.nl/`.

TU Delft

Preface

Arguably the largest existential threat to our civilization right now is climate change. The European heat wave of this year was unusual, but is expected to become the norm by the middle of this century as global temperatures are steadily increasing. Meanwhile, coastal cities are under threat of being inundated due to melting ice sheets. I hope this thesis contributes towards the technology that can solve the crisis.

Over the course of this MSc thesis, however, I have come to realize that climate change is no longer principally a technological problem, but rather a political problem intertwined with economics. The necessary technology is already here and at a very low price. What remains to be done is for masses of society to override the interests of the few who stand to benefit from a slow transition to green energy, and to start investing heavily in a renewable future.

Nevertheless, the product of this thesis, a fuel cell drone for measuring soil carbon, could be part of this renewable future. As you'll see in one of the chapters, it is important to maintain a healthy level of soil carbon, the first step of which would be monitoring. In addition, I have learned quite a lot working on this thesis, as it encompasses several topics: fuel cells, drone design, and LiDAR. I hope you will learn something as well reading this thesis.

I'd like to acknowledge the support and guidance of my supervisors at various points during the project.

I thank the Technical University of Delft for providing high quality education at a low cost.

And last but certainly not least, I am deeply grateful to the working class of this world for keeping our infrastructure running smoothly, without which modern society would not be possible. Their contributions are worth much more than what they're given credit for.

Louis Cheung
Delft, July 2019

Contents

1

Summary

We have set out to develop a drone, based on the existing Delftacopter, capable of soil monitoring via LiDAR remote sensing. The battery was to be replaced by a fuel cell system in order to extend the range threefold to 180 km. Unfortunately, the ultimate design is likely unfeasible.

Agriculture requires healthy soil and monitoring soil health is fundamental to its maintenance. Soil organic carbon in particular provides energy to the soil's microorganisms, and is beneficial to water and nutrient retention. In addition, storing carbon in the soil is a form of carbon sequestration, which has become interesting due to the rising levels of carbon dioxide in our atmosphere. Monitoring soil organic carbon is therefore the goal of the drone design.

The fuel cell system is a 650 W hydrogen fuel cell by Intelligent Energy with a mass of 1290 g, which will be replacing the battery in the base design. Fuel tanks that were considered suitable are the 450 g, 0.5 L, 500 bar and 1350 g, 3 L, 300 bar fuel tanks by Meyer. It was found that one 1350 g and two 450 g fuel tanks were necessary to achieve the desired range of 180 km. However, after more careful drag estimates, this configuration turns out to be too heavy. 4 450 g fuel tanks remains feasible. Results below are based on this amount of fuel tanks.

The incorporated LiDAR sensor is one by Velodyne, namely the Puck LITE, with a specified range of 100 m. The LiDAR sensor has a firing cycle of 55.296 µs, almost 20 kHz. Based on previous studies that used LiDAR to measure soil organic carbon, it has been established that a density of 5 data points per square meter is required.

From our LiDAR parameters it turns out that the optimal flight altitude is 27.5 m above the surface that is to be measured, with a rotation rate of 10 Hz for the LiDAR sensor, when flying at a speed of $20\,\mathrm{m\,s^{-1}}$. With a flight distance of roughly 116 km at $22.5\,\mathrm{m\,s^{-1}}$ (111 km at $20\,\mathrm{m\,s^{-1}}$), an area of $21.8\,\mathrm{km^2}$ per flight can be scanned.

2

General Introduction

2.1. Climate Change

On 8 October 2018, the Intergovernmental Panel on Climate Change (IPCC) published another Special Report[23] documenting the current and future status of climate change and its effects, and detailing policy proposals. Global mean surface temperature (GMST) in the period 2006–2015 has increased 0.87 ± 0.12 °C relative to 1850–1900 due to anthropogenic CO_2 emissions. The report compares the effects of a 1.5 °C and a 2 °C warming in the GMST. As can be expected, the latter will have stronger repercussions on the climate than the former, including:

- Higher mean temperature on most land and sea.
- Higher extreme temperatures in inhabited regions, especially in the tropics.
- More frequent and/or intense precipitation in some regions.
- More frequent and/or intense drought in other regions.

Further consequences of a 1.5 °C rise in GSMT are as follows (with consequences from a 2 ° rise between brackets):

- Sea level rise of 0.26m to 0.77m (an additional 0.1m).
- Loss of biodiversity, and biodiversity-related risks such as forest fires and spread of invasive species.
- Negative impact on ecosystems (50% more ecosystems affected), including a 70–90% (>99%) decline of coral reefs, ocean acidification affecting the livelihood of many species such as algae and fish.
- Decreased productivity of fisheries: 1.5 megatons (3 megatons) reduction in global annual catch.

Direct impacts on humans include:

- risks to food and water security.
- increased heat-related deaths.
- spread of diseases, such as malaria.
- hampered global economic growth due to all aforementioned impacts.

In order to achieve the 1.5 °C warming target, global CO_2 emissions have to decrease 45% by 2030 from 2010 levels, and reach net zero emissions by 2050. The remaining carbon budget that corresponds to said reduction is around 500 gigatons[1] of CO_2 or 136 gigatons of C.

A crisis of this scale can only be averted through a far-reaching transformation of all industries. According to the IPCC, necessary technologies already exist and include: electrification, hydrogen technology, sustainable bio-based feedstocks, product substitution, and carbon capture, utilization and storage. Hydrogen fuel cells and carbon storage in soil form the main topics of this thesis.

[1] One (metric) gigaton equals one petagram or 1 Pg

2.2. Soil Carbon

Not to be overlooked is the fact that the IPCC calculations assume carbon dioxide removal of several hundred gigatons over this century, but does not state the method for reaching this. One environmentally friendly solution is to store carbon in the ground with the co-benefit of improving soil health.

The global amount of carbon in the soils has been estimated at around 2200 Pg in the upper 100cm of soil[9]. 320 Pg of soil carbon has been lost due to agriculture since its advent[40], around 140 Pg of which was lost after 1850[15]. To put this into perspective, global carbon emissions (in the form of CO_2) from burning fossil fuels was around 10 Pg of carbon per year in 2017.[2] Carbon storage in soil, or carbon sequestration, therefore has the potential to both improve soil health and mitigate climate change[28].

2.3. Soil Monitoring by Drone

Since their commercialization, drones have been used for monitoring other aspects of soil. For example, photographic data can be taken from a drone in order to understand soil erosion[37][36]. Such information is of interest to urban and land planners as eroded soil increases flood risks[37]. Another basic soil parameter is humidity which can also be and have been measured by color images[25]. Irrigation is timed based on this information. More information about soil health can be obtained by soil sampling, and even in this area drones can be used to make the process more efficient[22].

In the Netherlands, agricultural projects are ongoing which employ drones supported by 5G.[3] Such data can help in optimizing soil usage. Healthier soil allows more crops to grow. A large agricultural field will consist of areas with better or lower health, and seeds can be sown accordingly. Additionally, use of water and pesticides can be reduced with more precise and detailed knowledge of local moisture and pesticide levels.

2.4. Soil Carbon Monitoring by LiDAR

In this thesis, the method of measuring soil health is via soil carbon, and this is to be done by Light Detection and Ranging (LiDAR). LiDAR can determine distances to objects by bouncing light off the object and measuring the time the light takes to return. In such an application LiDAR would be used to measure tree size properties or reflectance of vegetation at the frequency of the laser. We will go into this in Chapter 5.

LiDAR equipment used to be quite bulky and so was equipped only on aircraft and helicopters. But the size and weight have come down to the point that it is possible to mount a LiDAR sensor on a drone. Conveniently, costs have decreased as well.

2.5. Thesis Goal and Structure

This thesis' objective is to design a drone which will be used to measure soil carbon and will be powered by a fuel cell. The Delftacopter[4] is used as a starting point. This drone is at the moment powered by batteries. The expectation is that the range can be tripled by replacing the batteries with a hydrogen fuel cell and fuel tank.

By having a drone that can quickly measure large areas of soil, it is hoped we will manage these carbon sinks properly and use them for carbon sequestration. The drone itself does not pollute the environment as it only emits clean water as a waste product.

This project covers three main topics: the fuel cell, the Delftacopter, and the LiDAR system. One chapter is dedicated to each topic. Chapter 3 describes the chemistry of a PEM fuel cell. In this chapter we will also select the fuel cell and fuel tank. Chapter 4 introduces the Delftacopter and its performance and efficiencies. Chapter 5 is about why and how we measure the soil. Chapter 6 goes into the performance of the LiDAR system. These chapters culminate in the last chapter where all three components are integrated into a final design.

A small but significant part of the thesis was written 6 months before the rest. The structure may therefore not be ideal. Chapter 4 for example ends rather abruptly before continuing in the last chapter. The choice for the fuel cell in Chapter 3 may not be clear until the end.

Lastly, a note on abbreviations and symbols: the first time an abbreviation is used, it is written in bold for easy reference. Some of the symbols may overlap between chapters, as different fields of research may use the same letter for their own designations. For example V can refer to the fuel cell voltage or the flight speed

[2] `https://www.epa.gov/ghgemissions/global-greenhouse-gas-emissions-data` Retrieved on 1 Dec 2018.
[3] `https://www.kpn.com/zakelijk/internet-of-things/smart/farming/en.htm`, Retrieved 7 August 2019
[4] `http://www.delftacopter.nl/`

of the drone. This should not be a problem however, since these symbols are used in different chapters and contexts.

3

Fuel Cell

3.1. Introduction

The purpose of a fuel cell is to generate electrical energy from chemical energy, most often of hydrogen. The history of the hydrogen fuel cell began when Sir William Grove in 1839 described the first device capable of producing electricity by combining hydrogen and oxygen. Due to competition with the energy dense fossil fuels, first coal then oil, development of the fuel cell was sluggish and it took almost a century before the technology reached maturity[5]. In 1959, Francis Thomas Bacon produced the first fuel cell that would be adopted by NASA[43]. Nowadays, hydrogen fuel cells are gaining interest for their potential in providing clean energy with high density, and are thus being implemented in transport vehicles, such as cars, trams, and trains.[1][2][3] The main competitor in the field of electricity storage and generation is the battery. When considering mobile applications, some may favor fuel cells for their higher energy density and hence range, while others will favor batteries for their higher efficiency and hence less waste heat. In terms of durability, the fuel cell has a large advantage over batteries, as the latter suffers from a limited cycle lifetime, leakage and corrosion[43].

For our purpose of taking measurements over large areas on the Delftacopter, it is economical to have a long flight duration and hence range. Since hydrogen has a higher energy density than batteries, it makes sense here to use a fuel cell, especially considering that the additional waste heat production, relative to a battery-powered drone, is easily dissipated in the surrounding air.

Note that the original goal in this chapter was to dive into the operations of a fuel cell in order to modify it for its implementation in our drone. In the end, no modifications to the fuel cell were made. The following two sections have therefore lost some of their relevance, though may still serve as an introduction to the topic.

3.2. From Hydrogen to Electricity

When solving problems in a particular system, one has to first understand its underlying mechanisms. In this section, the basic principles of a hydrogen fuel cell are explained, following the book [31].

Schematic diagrams of the well known proton exchange membrane (PEM) and alkaline fuel cells are shown in Figure 3.1[4,5]. In a PEM fuel cell, reactions at the anode and cathode are:

$$H_2 \longrightarrow 2H^+ + 2e^- \tag{3.1}$$

$$O_2 + 4e^- + 4H^+ \longrightarrow 2H_2O \tag{3.2}$$

The membrane carries protons towards the cathode where it reacts with oxygen to form water.

[1] https://www.hyundai.com/worldwide/en/eco/nexo/because-of-you Retrieved on 4 Dec 2018

[2] http://ballard.com/about-ballard/newsroom/market-updates/tangshan-railway-vehicle-company-commences-hydrogen-powered-tram-tri Retrieved on 4 Dec 2018

[3] https://www.alstom.com/coradia-ilint-worlds-1st-hydrogen-powered-train Retrieved on 4 Dec 2018

[4] https://commons.wikimedia.org/wiki/File:PEM_fuel_cell.svg Retrieved on 6 Dec 2018

[5] https://www.researchgate.net/figure/Schematic-representation-of-an-alkaline-fuel-cell-AFC-2_fig2_268811074 Retrieved on 6 Dec 2018

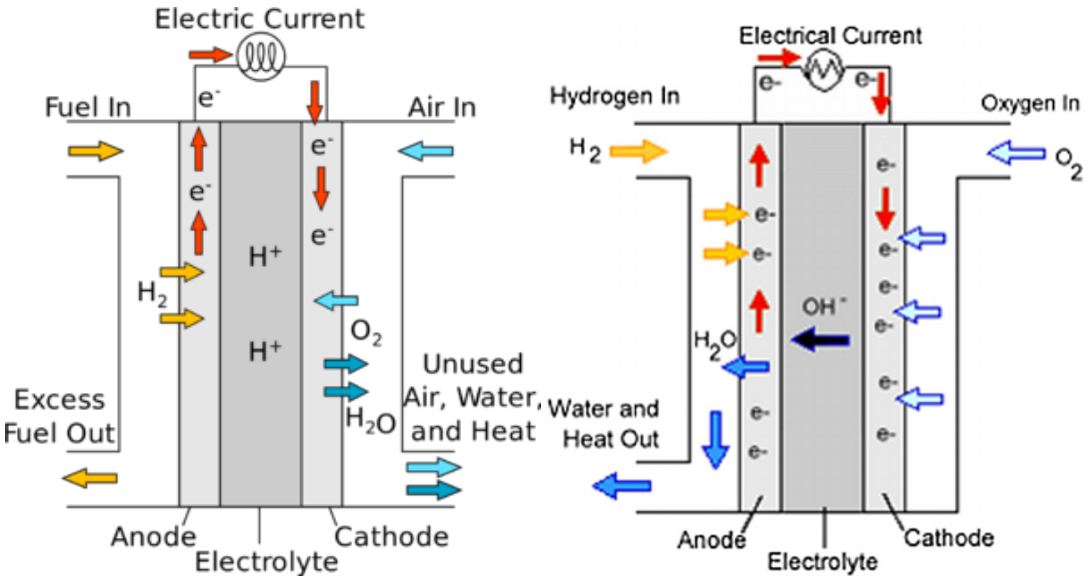

Figure 3.1: Schematics of a standard PEM fuel cell (left) and alkaline fuel cell (right).

For an alkaline fuel cell, anode and cathode reactions are:

$$H_2 + 2OH^- \longrightarrow 2H_2O + 2e^- \tag{3.3}$$

$$O_2 + 4e^- + 2H_2O \longrightarrow 4OH^- \tag{3.4}$$

The fuel cell is called alkaline because the membrane carries hydroxyl ions. The overall reaction of both cells comes down to:

$$2H_2 + O_2 \longrightarrow H_2O \tag{3.5}$$

This reaction sets an upper limit for the output voltage via the difference in Gibbs free energy of formation of the products and reactants, Δg_f:

$$E = -\frac{\Delta g_f}{2F} \tag{3.6}$$

where $F = 96485$ C/mol is Faraday's constant. Under standard ambient temperature and pressure, $\Delta g_f = -237.1$ kJ/mol, which gives $E = 1.23$ V. Standard state is defined as $T = 25°C$ and $P = 1$bar. Changing the pressure will change the Gibbs free energy, according to the Nernst equation:

$$\Delta g_f = \Delta g_f^0 - RT \ln\left(\frac{a_{H_2} \cdot a_{O_2}^{1/2}}{a_{H_2O}}\right) \tag{3.7}$$

$$\Rightarrow E = -\frac{\Delta g_f^0}{2F} + \frac{RT}{2F} \ln\left(\frac{a_{H_2} \cdot a_{O_2}^{1/2}}{a_{H_2O}}\right) \tag{3.8}$$

$$a_{H_2} = \frac{P_{H_2}}{P_{H_2}^0} \tag{3.9}$$

where a_i is the activity of species i, defined for gases as the partial pressure divided by standard pressure $P^0 = 0.1$MPa, as in Eq. 3.9. For liquids the activity is approximately 1.

The current output of a fuel cell depends on its reaction rate. This rate is mainly limited by the activation energy of the reaction, which is the energy required for the reaction to start. Even though the reaction is exothermic, this energy still needs to be present. Under standard test conditions, the reaction rate may be too low.

Luckily, there are ways to increase the reaction rate, and hence current output. The main three are:

- Increase the temperature. This will shift the energy of the molecules higher up, allowing more of them to exceed the activation energy, hence increasing activity.

- Use a catalyst. This will hopefully lower the activation energy itself.
- Increase the electrode surface. This will allow more fuel to flow to where the reaction takes place.

The product of the output voltage and current is the final power output, and this will depend on the overall efficiency. Efficiency losses occurring in the fuel cell express themselves mainly in the output voltage, and they will be discussed in the next section.

3.3. Efficiency

In the previous section, three ways of increasing the current output were mentioned. There is of course a fourth way of influencing the current, namely by varying the fuel consumption. Fuel consumption, or utilization, is the main control parameter of a fuel cell, and is therefore quite important for the control and operation of a drone. In this section, we briefly go through the factors influencing the efficiency at different current output rates, which is proportional to fuel consumption.

There are four loss mechanisms:

- Activation losses due to the activation energy as mentioned previously. Higher temperature leads to a more active cell (higher exchange current), reducing the activation losses.
- Fuel crossover losses due to the crossover of fuel through the membrane. This effect is usually negligible.
- Ohmic losses due to electrical resistance of electrons in the wires and of ions in the electrolyte.
- Mass transport, or concentration, losses due to the limitations of fuel transport to the more distant parts of the electrode. This leads to lower concentration and hence activity, thereby lowering the voltage via Equation 3.7.

Putting them all in one formula gives:

$$V = E - \Delta V_{\text{act}} - \Delta V_{\text{fuel}} - \Delta V_{\text{ohm}} - \Delta V_{\text{trans}} \tag{3.10}$$

$$= E - A\ln\left(\frac{i+i_n}{i_0}\right) + m\exp(ni) \tag{3.11}$$

where $A = \frac{RT}{2\alpha F}$ is a constant describing the slope of the voltage loss (overvoltage) versus current. α varies very little among known materials. i_n is the current representing fuel crossover. m and n are empirical parameters that describe the mass transport losses.

From the equation, you can already see that the voltage decreases for higher current outputs. The general shape is like Figure 3.2[6].

3.4. Fuel Tank Selection

A small light-weight hydrogen fuel tank suitable for drones is the Meyer HDRX-005-500, which weighs only 450 grams.[7] Its volume is 0.5L and can store hydrogen at 500 bar. We will see in Chapter 7 that the HDRX-030 will also be useful. This one weighs 1.3 kg and stores 3 L of hydrogen at 300 bar. These fuel tanks were chosen as no other fuel tanks could be found that fitted our tight weight budget.

Hydrogen weighs 30.811 kg/m^3 at 25 degrees Celsius and 500 bar, and 20.538 kg/m^3 at 25 degrees Celsius and 300 bar.[8] The 0.5L fuel tank therefore contains 15.4g of hydrogen, and the 3L tank contains 61.7g, or 4 times as much. The Gibbs free energy of formation of (liquid) water is −237.14 kJ/mol[44], therefore the 0.5L fuel tank can store 1.812 MJ or 503.3 Wh of energy.

[6] https://www.springer.com/cda/content/document/cda_downloaddocument/9783319255965-c2.pdf?SGWID=0-0-45-1544891-p177747467 Retrieved on 9 Dec 2018

[7] http://meyer.cd/copv/, Retrieved 19 Jan 2019

[8] https://h2tools.org/hyarc/hydrogen-data/hydrogen-density-different-temperatures-and-pressures Retrieved on 16 Dec 2018.

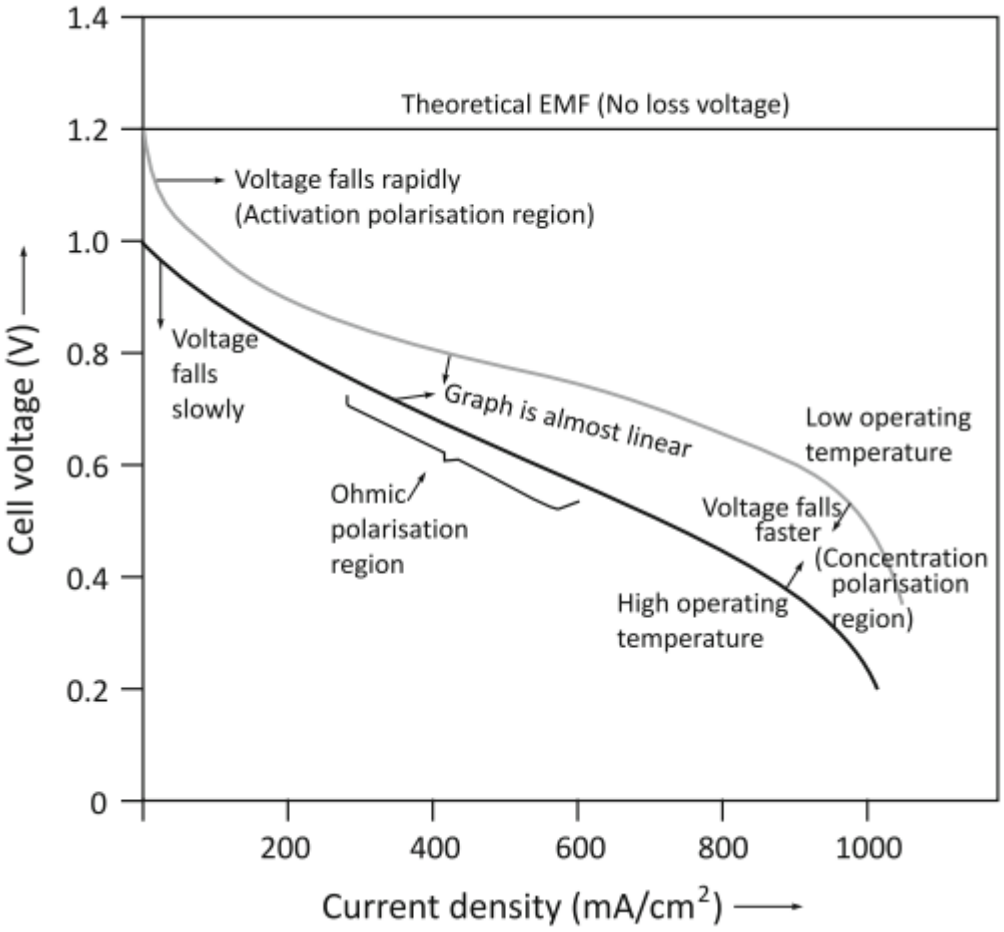

Figure 3.2: Voltage versus current for a fuel cell operating at high temperature and low temperature, showing the main three loss mechanisms and the current regimes in which they are the most significant. Activation losses affects the voltage mostly at low currents; Ohmic losses at medium currents; and mass transport losses at high currents.

Fuel	Specific Energy		Density
	[Wh/L]	[kWh/kg]	[kg/m^3]
Hydrogen (500 bar, 25 °C)	1006.8	32.68	30.811 (930.8)
Methanol	4690	5.922	792
Ethanol	6280	7.959	789
Formic Acid	2086	1.710	1220

Table 3.1: Density and specific energy of some substances used in fuel cells. For hydrogen, the lower value is hydrogen-only, and the higher value between brackets includes the mass of the fuel tank from Section 3.4.

3.5. Other Types of Fuel Cells

In Section 3.2, we have already seen the working principles of two main types of fuel cells: PEM and alkaline.

Some fuel cells use charge carriers other than H^+ or OH^-. For example the charge carrier in a solid oxide fuel cell is O^{2-} and in a molten carbonate fuel cell ${CO_3}^{2-}$. These fuel cells also operate at very high temperatures of several hundred °C, which increases their chemical activity and thus efficiency. However, to maintain such temperatures on a small drone is not feasible, due to weight restrictions.

Other types of fuel cells operate on less conventional fuels such as phosphoric acid, formic acid, methanol, or ethanol. Their main advantage is high volumetric energy density owing to their high boiling point relative to hydrogen. The disadvantage is low gravimetric density. In Table 3.1, some properties of these fuels are shown. Even though the density of the fuel tank plus hydrogen is 930.8 kg/m^3, which is higher than for some of the other fuel. The energy density of hydrogen is far higher than the other fuels.

This advantage of hydrogen is slightly diminished when we take into account weight loss during flight as fuel is consumed. The weight of the fuel tank is only around 450 grams. If this is instead entirely used for a fuel which is expended during a mission, it would roughly amount to 10% reduction in the weight after a full length mission. The difference in energy density (kWh/kg) between hydrogen and the other fuels is almost one order of magnitude. Hence, even when taking weight loss into account, hydrogen remains the best choice for the Delftacopter.

3.6. Fuel Cell System Selection

A fuel cell designed for drones is the 650 W fuel cell by Intelligent Energy[9]. Its mass without the emergency battery is 1060 g, and 1290 g with battery. Its fuel is hydrogen, but the fuel cell efficiency is not given.

This fuel cell is a PEM fuel cell, which generally have a quick start-up time. This is of course necessary for drone operations, as a drone needs to be able to throttle quickly during take off and landing. The efficiency of a PEM fuel cell can be around 50%[7].

The fuel cell was chosen for its power to weight ratio. Other options were less attractive in this regard: the Aerostak 500 W (1300 g), and Ballard 600 W (1800 g).

[9] https://www.intelligent-energy.com/uploads/product_docs/650W_datasheet_AwPJVHR.pdf

4

Delftacopter

4.1. Introduction

There are two main classes of aircraft. One is the airplane, which generates lift from its fixed wings, and is therefore capable of long high speed cruise flight. As a disadvantage, however, they require a runway. Another is the helicopter, which generates lift from rotors. Its advantage is the ability to hover, take off from and land almost anywhere, and perform maneuvers within a small area, but it is not able to cover distances as long as that of an airplane. A vehicle optimized for both modes of flight could be operated efficiently in places without runways, such as ships, cities, and forests, with a range that is much improved over the helicopter. It would open up new possibilities such as the delivery of goods or supplies to remote locations, the inspection of roads, power grids or the quality of soil without runways in the vicinity.

Aircraft designs that seek to combine the advantages of airplanes and helicopters are called hybrid aircraft, which include both manned and unmanned vehicles. Such designs typically involve large rotating parts, such as movable rotors and engines or even movable wings, making them complex, heavy, and more susceptible to mechanical failure.

One of the first hybrid unmanned aerial vehicles (**UAV**) is the tail-sitter, which was a notable improvement in that regard. As the name suggests, the tail-sitter rests on its tail at the start and end of its operation. This UAV rotates its entire body to switch between flight modes and thus requires fewer moving parts[39].

The Delftacopter is based on the tail-sitter concept. Originally, it used batteries as its energy source. When the batteries are replaced by the hydrogen fuel cell from the previous chapter, its performance should improve.

This chapter describes the original battery-powered Delftacopter and discusses the consequences of using the fuel cell and fuel tank selected in the previous chapter.

4.2. Design Challenge

The Delftacopter was designed in an attempt at the Outback Medical Express UAV Challenge 2016. The challenge took place in Australia and the objective was the retrieval of a blood vial over a distance of 30 km at a location that is hypothetically surrounded by floodwater and thus not easily accesible by land.

During the challenge, all hardware was working properly. Unfortunately, the Delftacopter team was not able to make a return flight. Some issues in software and ground control arose, which were a result of the limited allowed preparation time on site. In any case, this accident should not impact the results of this thesis.

4.3. Rotor and Motor Design

The Delftacopter design as was used during the medical express challenge and shown in Figure 4.1, consists of two delta wings with two fins attached at the ends, which provide stability when resting on the ground, while lowering sensitivity to lateral wind and minimizing conditions of stall[16]. Its wing span and wing area are 1.5m and 0.496m^2.

There is another complication when optimizing for the flight modes, cruise and hovering, apart from the one described in the Introduction. This is related to the main rotor, namely that during hovering, a low pitch

Figure 4.1: The Delftacopter during hovering.

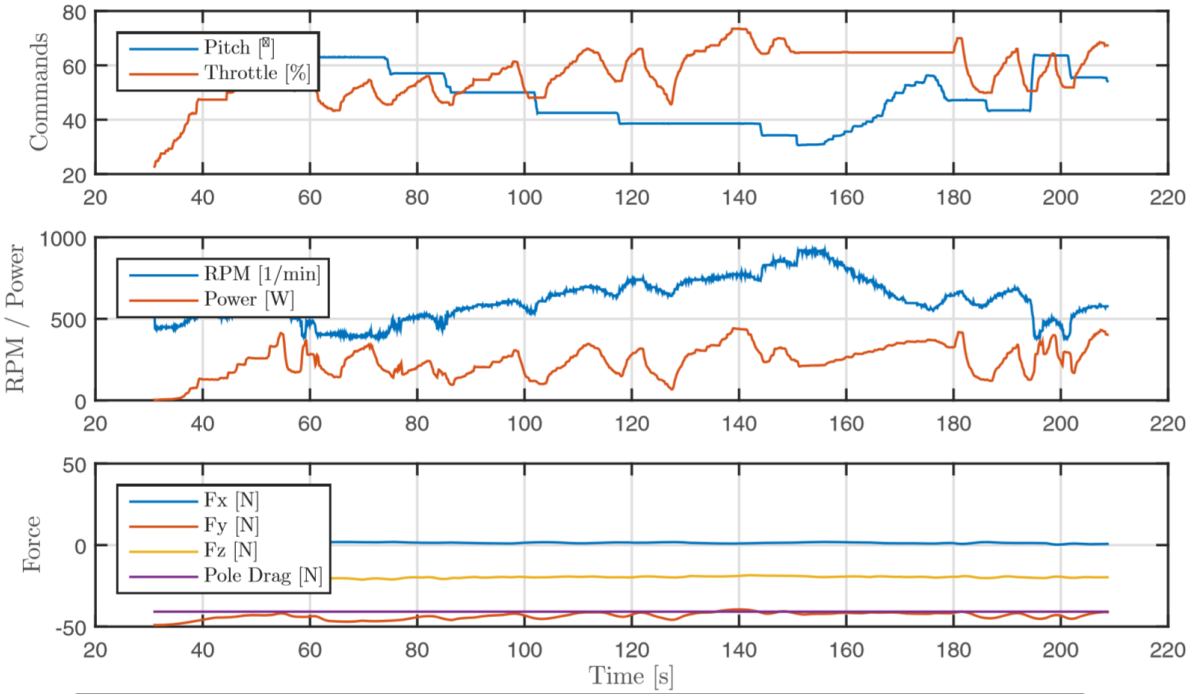

Figure 4.2: Wind tunnel test of Delftacopter at 19 m/s.

MTOW	4.5 kg
Wing area	0.496 m^2
Wing loading	8 kg/m^2
Span	1.54 m
Length	0.6 m
Height	0.4 m
Cruise speed	23.8 $m\,s^{-1}$ at 450 W
Maximum speed	30 $m\,s^{-1}$
Flight distance	60 km
Hover climb	660 W
Hover descent	550 W
Main battery	179.2 Wh
Battery weight	1.8 kg

Table 4.1: Overview of Delftacopter properties

angle and high rpm is desired, whereas during cruise, a high pitch angle and low rpm would be most efficient. The Delftacopter design has therefore implemented variable pitch rotors. For optimal efficiency, a 10° pitch angle at 1500 rpm is used during hovering, and 50° at 500 rpm during cruise. Different flying speeds can be reached by changing the pitch, while keeping the rpm constant.

Powering the Delftacopter is a 900 watt *iPower MT8017*, which weighs 385 grams and is fed by 18 lithium-polymer cells. The motor and batteries are to be replaced by a hydrogen fuel cell and a fuel tank with higher energy capacity.

Theoretical calculations concluded that the optimal cruise speed is around 19 m/s. Performance at this speed were then measured in a wind tunnel test, Figure 4.2. Important conclusions were the following:

- An RPM of 700 is required to obtain a speed of 19 m/s.
- Efficiency drops below 900 RPM, at a speed of 19 m/s.
- Efficiency drops sharply above 22 m/s due to engine limitations. The practical maximum speed is thus about 22 m/s.

In the end, it was decided that the Delftacopter should operate at an RPM above 1000 for cruise flight, since this would enable faster adaptation between hover and cruise. The flight speed can still be controlled by changing the pitch of the blades.

4.4. Flight Performance

In the subsections below, some flight characteristics of the Delftacopter are calculated, such as minimal and maximal speed, and their theoretical power consumption. This will be crucial for determining the flight time per filled tank and thus the area that can be scanned per flight. The most recent and realistic data on the current Delftacopter that I have is provided in Table 4.1. In the following section we will use the MTOW of 4.5 kg as the mass of the drone. In Chapter 7 we will come back to this.

4.4.1 Minimal speed

The maximum lift at a certain speed V that a single wing can produce is

$$L_{\max,s} = \frac{1}{2} C_{L,\max} \rho S V^2 \tag{4.1}$$

with S the surface area of the wing, $C_{L,\max}$ the maximum lift coefficient. For a biplane, the lift is slightly reduced due to aerodynamic interference between airflows of the stacked wings[34].

$$L_{\max,b} = 0.9 \cdot 2 L_{\max,s} \tag{4.2}$$

Without hovering capabilities, this maximum lift will determine the minimal speed, since, below a certain speed, the wings will not produce enough lift to keep the drone in the air. Let's call this speed, $V_{\min}$. At lower speeds or even zero speed, the Delftacopter can use its hovering capability to stay in the air. This flight mode,

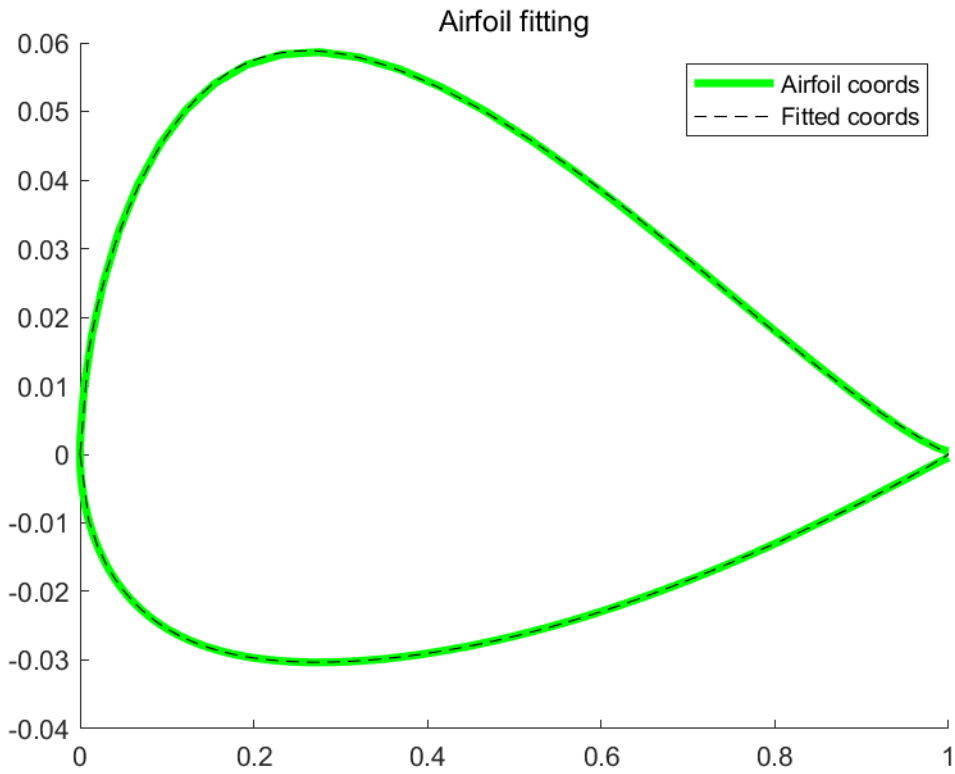

Figure 4.3: PW51 Airfoil of the two wings on the Delftacopter.

however, requires significantly more power than cruise flight. $V_{\min}$ importantly draws the line between the two flight modes, and in the following paragraphs, we will try to estimate $V_{\min}$.

In steady level flight, the lift counterbalances the weight

$$L = W \tag{4.3}$$

Putting the above three equations together

$$W = 0.9 \cdot 2L_{\max,s} = 0.9C_{L,\max}\rho S V^2 \tag{4.4}$$

$$\Rightarrow V_{\min} = \sqrt{\frac{W/S}{0.9C_{L,\max}\rho}} \tag{4.5}$$

The minimal speed, $V_{\min}$, is a function of air density ρ and maximum lift coefficient $C_{L,\max}$. At higher altitudes, ρ decreases and $V_{\min}$ increases. In words, it is more difficult to stay in the air if the air becomes more dilute.

C_L is a function of the angle of attack α.[1] At $\alpha = 0$, $C_L = 0$ for a symmetrical airfoil. However, some airfoils, such as the one used in the Delftacopter (Figure 4.3), are not symmetrical, but cambered. This means that the upper part is bent upwards, which accelerates the air leading to a lower pressure. The pressure difference above and below the wing creates lift, even at $\alpha = 0$. Another lift-creating mechanism is of course changing the angle of attack. A larger angle of attack intuitively increases the lift, as more air pushes against the lower part of the wing. At some angle of attack, airflow above the wing starts to separate, creating both an increase in drag and a reduction in lift. This is called the critical angle of attack or stall angle.

Hence, by definition, the stall angle provides the maximal lift, which, as argued before, is directly related to the minimal flight speed. But how do we find the stall angle?

[1] The angle of attack is the angle between the airflow and the airfoil's chord. An airfoil is a cross section of the wing. Its chord line runs straight from the leading edge to the trailing edge.

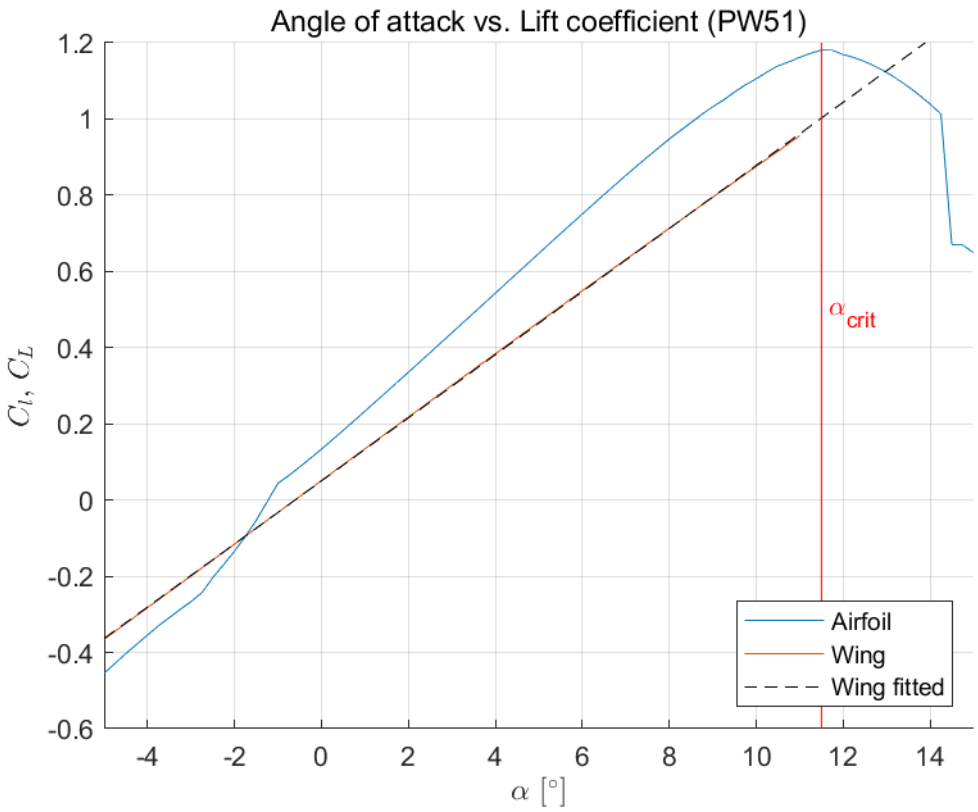

Figure 4.4: XFoil data for the sectional lift coefficient C_l, and Q3D data for the total lift coefficient C_L. The dotted line shows a linear fit to the Q3D data. Lift coefficients increases linearly until it approaches α_{crit}, the angle of the maximum sectional lift coefficient. The wing suffers from vortices at the tip, which the airfoil does not.

Calculating stall angles is not as straightforward and in fact requires complex modeling, whether in two or three dimensions. In 2D models, the wing is considered to be infinite, such that the problem can be viewed in a flat plane. Effectively, the characteristics of the airfoil are modeled in this way. In reality, the wing is of course finite. An immediate consequence of this is that air can travel around the tip from the lower part of the wing to the upper part. This creates vortices which lower the total lift coefficient.

The effects described above can be seen in Figure 4.4, where the (sectional) lift coefficient of the airfoil C_l and the total lift coefficient C_L of the wing are shown. The package, Xfoil[17], was used for the airfoil, while the wing was analyzed with Q3Dsolver[33].

If we assume that the wing stalls at the same angle as the airfoil, then the maximum total lift coefficient is 1.0024 at an angle of $\alpha = 11.5°$. Generally speaking, a wing stalls at a slightly higher angle of attack compared to its airfoil. Hence, this lift coefficient is a lower estimate.

Now, with an estimate for the maximum total lift coefficient in our hands, we can go back to the formula for the minimal speed in Eq. (4.5), and find that the minimal speed is:

$$V_{\text{min}} = \sqrt{\frac{W/S}{0.9 C_{L,\text{max}} \rho}} = \sqrt{\frac{4.5 \cdot 9.81 / 0.248}{0.9 \cdot 1 \cdot 1.225}} = 12.7\,\text{m}\,\text{s}^{-1} \tag{4.6}$$

4.4.2 Power Consumption

In order to obtain the power consumption, we need to find the drag coefficient. According to basic aerodynamics, the drag coefficient, C_D, consists of two components: a constant term, $C_{D,0}$, encompassing friction or form drag, and a term which is a parabolic function of the lift coefficient, C_L, known as induced drag:

$$C_D = C_{D,0} + \frac{C_L^2}{\pi e \text{AR}} \tag{4.7}$$

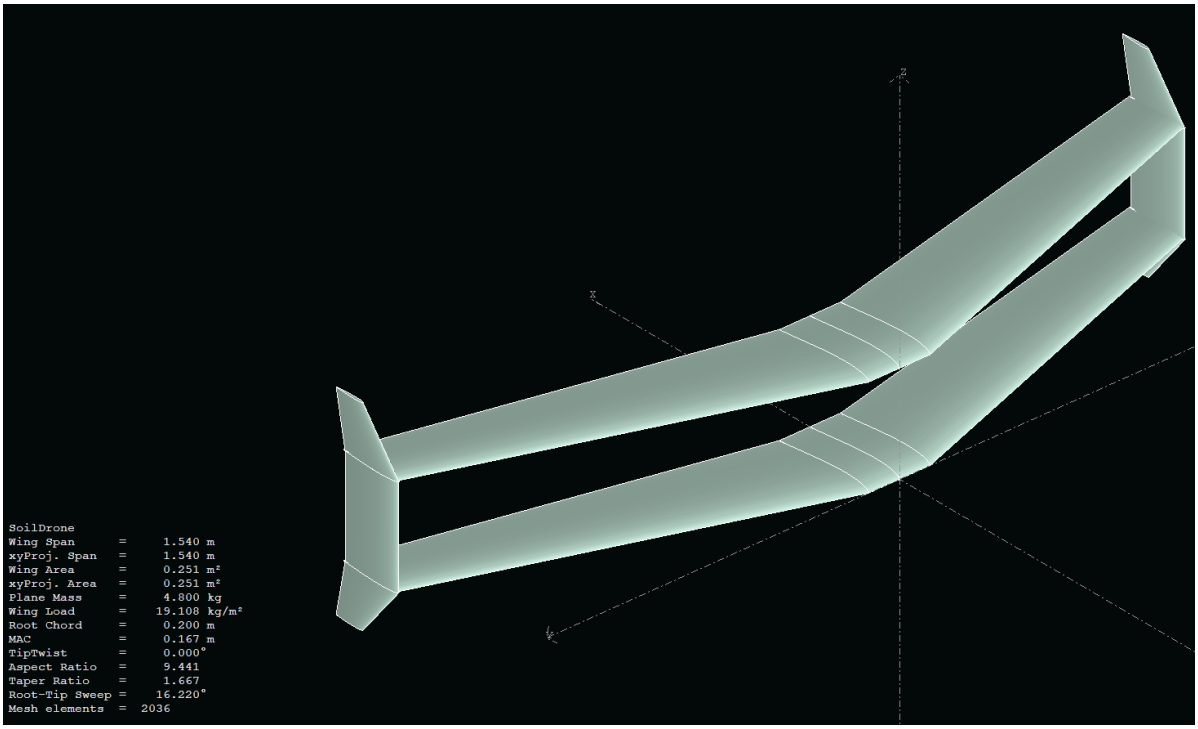

Figure 4.5: Delftacopter model in XFLR5.

with e the Oswald efficiency factor, which is 1 for an elliptical wing and less than one otherwise. AR is the wing aspect ratio. The total drag then is

$$D = \frac{1}{2} C_D \rho S V^2 \tag{4.8}$$

For a more detailed analysis, I have employed XFLR5, which is capable of 3D aerodynamic analyses. The PW51 airfoil was used for the two main wings, and the symmetrical NACA9 airfoil for the winglets at the tip, see Figure 4.5. The free flow speed was set at $23\,\mathrm{m\,s^{-1}}$, which leads to Reynolds numbers of around 200,000.

Unfortunately, I was not able to obtain any results when I included the fuselage. The following lift and drag estimates are therefore optimistic.

The XFLR5 analysis gives the relation between the drag and lift coefficient, also known as the drag polar, see Figure 4.6. The Reynolds number changes for different speeds, which mildly affects the drag polar. But neglecting this small effect, we can now calculate the power consumption at any flight speed.

The minimal flight speed in Eq. (4.6) was achieved at a lift coefficient of 1, which corresponds to a drag coefficient of 0.07. Drag, from Eq. (4.8), is then 3.43 N. To overcome this drag force, a power has to be supplied:

$$P_{\mathrm{minV}} = D V_{\mathrm{min}} = 3.43\,\mathrm{N} \cdot 12.7\,\mathrm{m\,s^{-1}} = 43.5\,\mathrm{W} \tag{4.9}$$

The same calculation of the power consumption can be made for different flight speeds. For a certain flight speed, a specific lift coefficient is required according Eq. (4.4). This lift coefficient then corresponds to a drag coefficient according to Figure 4.6. The drag force and (minimal) power consumption can then be calculated from Eq. (4.8) and Eq. (4.9).

The result is in Figure 4.7. You can see the characteristic parabolic shape. Initially, increasing the speed will lower the power consumption, since a lower lift coefficient and therefore drag coefficient is sufficient. After around $16\,\mathrm{m\,s^{-1}}$, power consumption quickly increases due to the quadratic relation between speed and drag.

4.4.3 Efficiencies

In order to calculate flight time we have to take into account the efficiency of converting the chemical energy in the hydrogen tank into forward thrust. There are three main efficiencies to be taken into account:

1. the efficiency of the fuel cell in converting hydrogen into electricity,

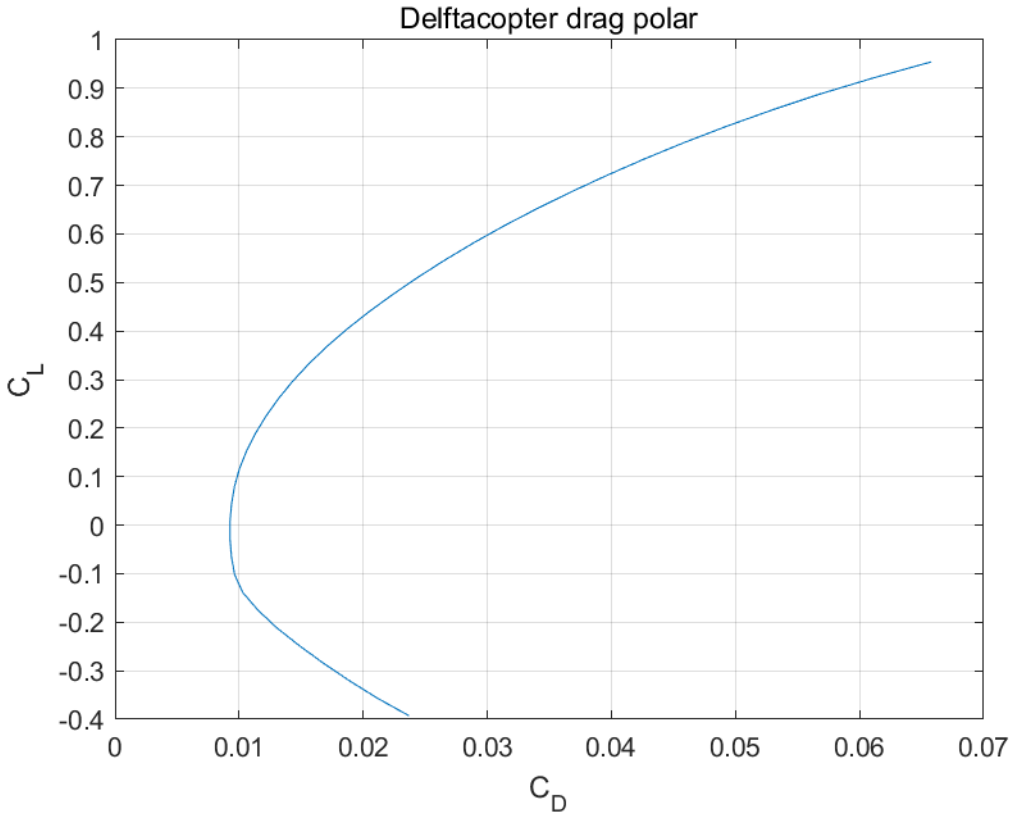

Figure 4.6: Lift and drag coefficients of the Delftacopter.

2. the efficiency of the engine in converting the electricity into shaft power, and

3. the efficiency of the propeller in converting that power into forward thrust.

The efficiency of an electric motor is nearly constant over a large operational range[47]. In the following, I will simply assume a fuel cell efficiency of 50% and motor efficiency of 75%[2]. A fuel utilization factor of 0.95 was used.

As for the propeller, there are multiple theories which predict propeller efficiency. Following Chapter 6 in McCormick's *Aerodynamics, aeronautics, and flight mechanics*, the propeller efficiency can be roughly approximated with an actuator disc model, in which the propeller is modeled as a thin disc. Let us denote the speed of the incoming air by u_0,[3] and of the outgoing or ejected air by u_e. Then, the speed of air at the disc, u_{disc}, can be calculated using Bernoulli's equations. The result is that u_{disc} is the arithmatic average of the incoming and outgoing velocities

$$u_{\text{disc}} = \frac{u_e + u_0}{2} \tag{4.10}$$

Thrust produced by the propeller disc is mass flow, $\dot{m}$, times velocity change, Δu, at the disc:

$$T = \dot{m}\Delta u = \rho A_{\text{disc}} \frac{u_e + u_0}{2}(u_e - u_0) \tag{4.11}$$

$$= \rho A_{\text{disc}} \frac{u_e^2 - u_0^2}{2} \tag{4.12}$$

$$\Rightarrow \frac{u_e^2}{u_0^2} = \frac{2T}{\rho A_{\text{disc}} u_0^2} + 1 \tag{4.13}$$

[2] `https://www.energy.gov/sites/prod/files/2014/04/f15/10097517.pdf`, Retrieved 4 July 2019
[3] In the rest frame of the air, u_0 is the speed of the aircraft.

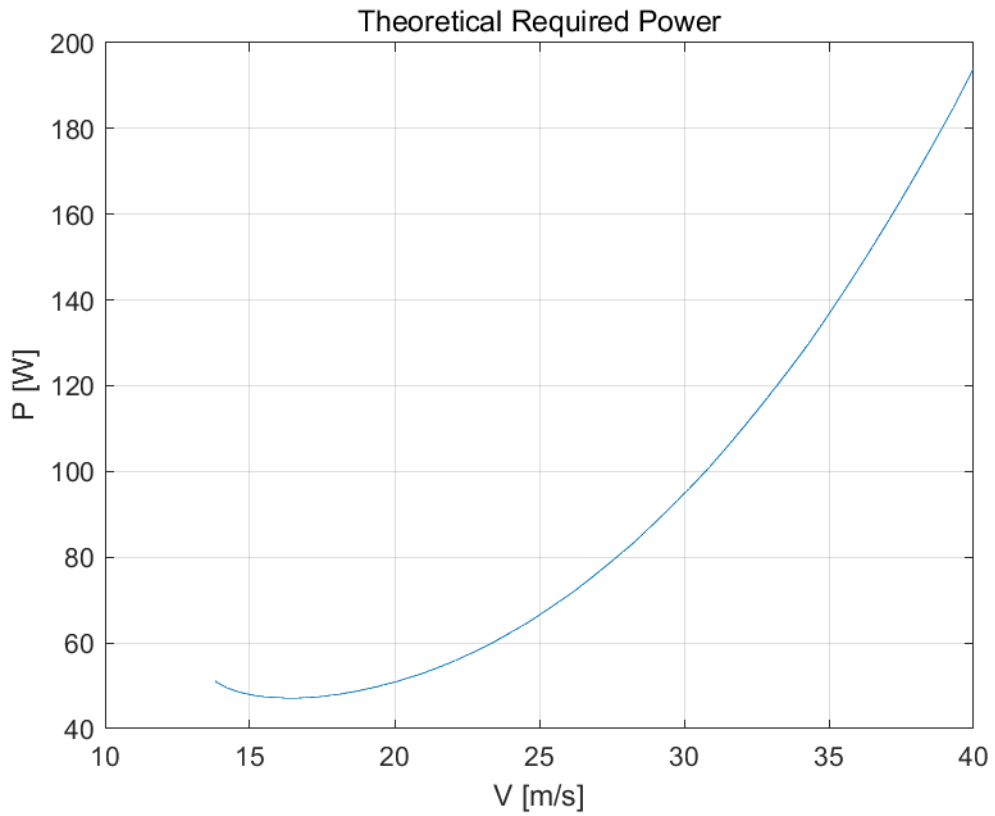

Figure 4.7: Minimal power required for a range of cruise speeds, based on a drag polar from XFLR5.

The air speed at the disc can be rewritten as

$$\frac{u_{\text{disc}}}{u_0} = \frac{u_e + u_0}{2}\frac{1}{u_0} = \frac{1}{2}\left(\frac{u_e}{u_0} + 1\right) \tag{4.14}$$

$$= \frac{1}{2}\left(\sqrt{\frac{2T}{\rho A_{\text{disc}} u_0^2} + 1} + 1\right) \tag{4.15}$$

Power delivered by the propeller is thrust times speed at the disc:

$$P = T u_{\text{disc}} = T u_0 \cdot \frac{1}{2}\left(\sqrt{\frac{2T}{\rho A_{\text{disc}} u_0^2} + 1} + 1\right) \tag{4.16}$$

Since Tu_0 is the useful power output, the efficiency is

$$\eta_{\text{prop}} = \frac{T u_0}{P} \tag{4.17}$$

$$= \frac{2}{1 + \sqrt{\frac{2T}{A_{\text{disc}} u_0^2 \rho} + 1}} \tag{4.18}$$

The end result is basically that the propeller efficiency drops due to the fact that the propeller is working on air at a speed of u_{disc} instead of u_0. We see that if $u_0 \to 0$, then $\eta_{\text{prop}} \to 0$, whereas if $u_0 \to \infty$, then $\eta_{\text{prop}} \to 1$. In reality, the efficiency does increase with speed, but reaches a maximum then quickly goes to zero. A more accurate theory, which can predict this result, is the blade element theory.

In the blade element theory, the propeller is no longer a simple flat disc, but its blades are modeled as well. Vortices at the tip and circular motion of the airflow are not considered. In this method, the lift and drag of each blade section are calculated, converted to thrust and power, and summed up. The calculations have

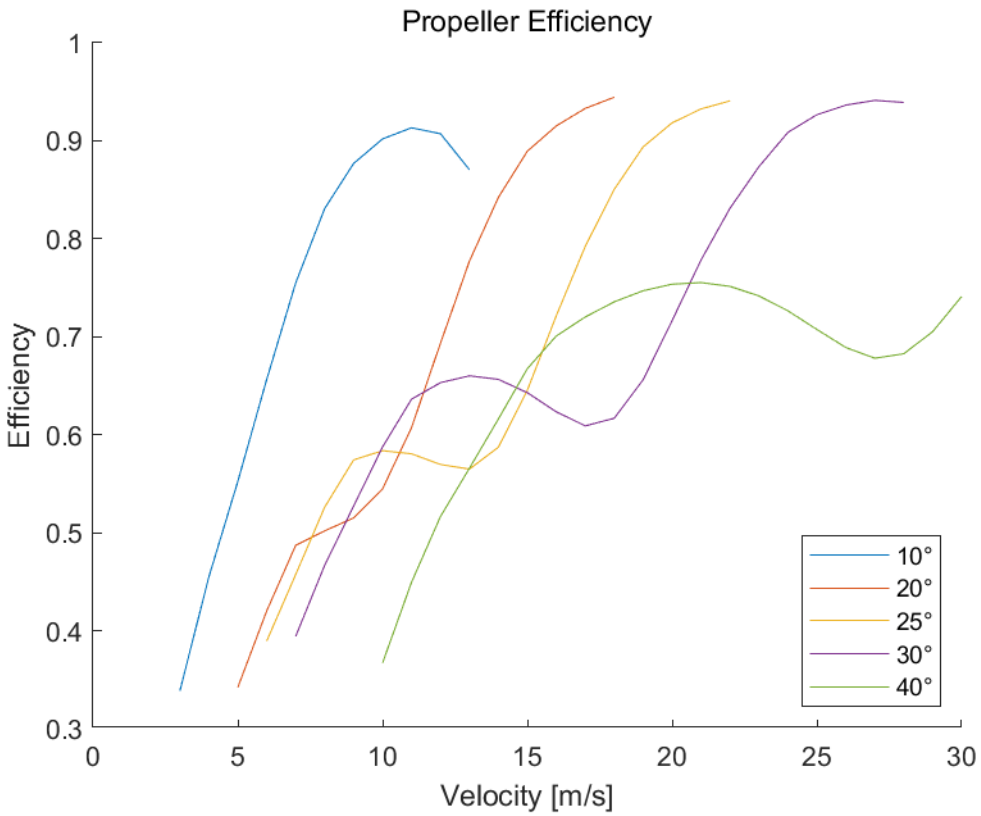

Figure 4.8: Propeller efficiency as a function of flight speed and blade pitch at 1140 RPM.

to be done iteratively,[4] since the effective angle of attack at the blade is a function of the induced air velocity at the blade, but this velocity depends again on that angle of attack.

After summing up all thrust and power contributions, $T = \sum \Delta T$ and $P = \sum \Delta P$, they are put into coefficients:

$$C_T = \frac{T}{\rho n^2 D^4} \tag{4.19}$$

$$C_P = \frac{P}{\rho n^2 D^5} \tag{4.20}$$

The efficiency becomes

$$\eta_{\text{prop}} = \frac{C_T}{C_P} J \tag{4.21}$$

with advance ratio

$$J = \frac{V}{nD} \tag{4.22}$$

The main conclusion from this is that propeller efficiency depends on the revolution per second n and the diameter of the diameter D.

With Xfoil data for the lift and drag coefficients of the propeller airfoil,[5] the efficiency can be calculated. I have calculated the propeller efficiency for several blade pitches. This pitch is added as a constant on top of the original propeller shape described in Table 1 in [16]. Results are shown in Figure 4.8, for a propeller rotation rate of 1140 RPM.

From this we can conclude that an added pitch of 25° is the optimal configuration for a speed of 22.5 $\mathrm{m\,s^{-1}}$.

[4] It is also possible to solve the equations analytically using a simplification called momentum-blade element theory, see McCormick Chapter 6 for more details.

[5] `http://airfoiltools.com/airfoil/details?airfoil=ma409sm-il`, Retrieved 17 March 2019

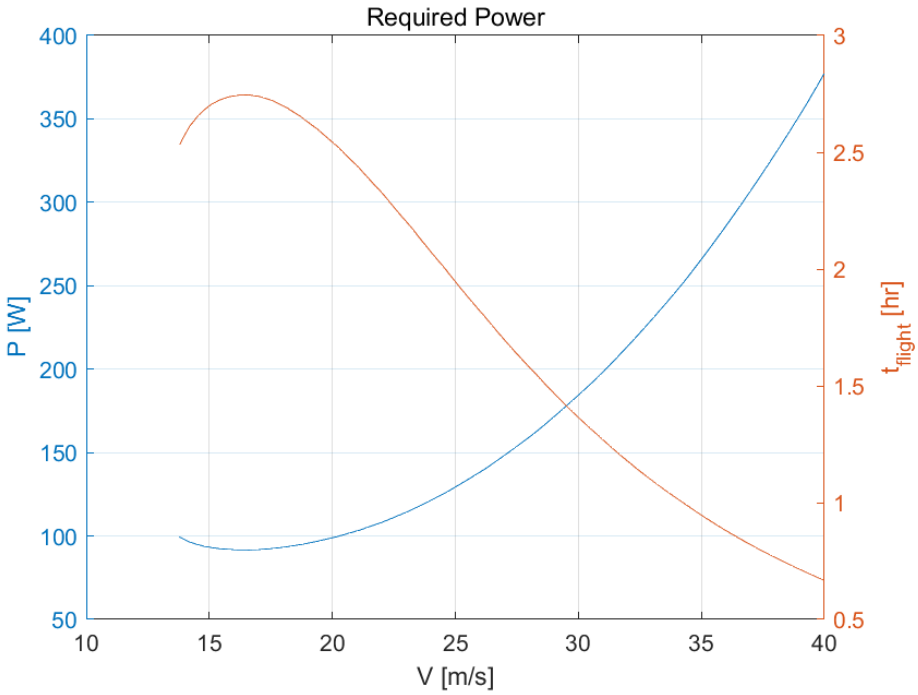

Figure 4.9: Power consumption including propeller and motor efficiency. The flight time is calculated by dividing the energy in the hydrogen tank by the power consumption, now also including the fuel cell efficiency.

4.4.4 Maximal Flight Range

If we assume that it's possible to change the pitch such that a propeller efficiency of 90% can be reached between the minimal and maximal speed, then we can update Figure 4.7 to account for the efficiencies discussed above to get Figure 4.9. The maximal flight time can then be easily calculated from the energy in the fuel tank (1.812 MJ, see Section 3.4). By multiplying the flight time with the flight speed, the maximal distance can calculated, see Figure 4.10.

The flight speed with lowest power consumption is around $16\,\mathrm{m\,s^{-1}}$, but the longest distance is reached at a speed of $21\,\mathrm{m\,s^{-1}}$.

Comparing these values for the power consumption with those in Table 4.1, these values are a factor four too low. If the power consumption at $23.8\,\mathrm{m\,s^{-1}}$ is scaled up to 450 W, by a simple multiplication at every speed, we get power consumptions and distances as shown in Figures 4.11 and 4.12. It turns out that one fuel tank will not be enough to fly further than 50 km.

In Chapter 7, we'll return to this and see what the effect is of adding more fuel tanks. First, we should determine the weight of the other crucial component: the LiDAR system.

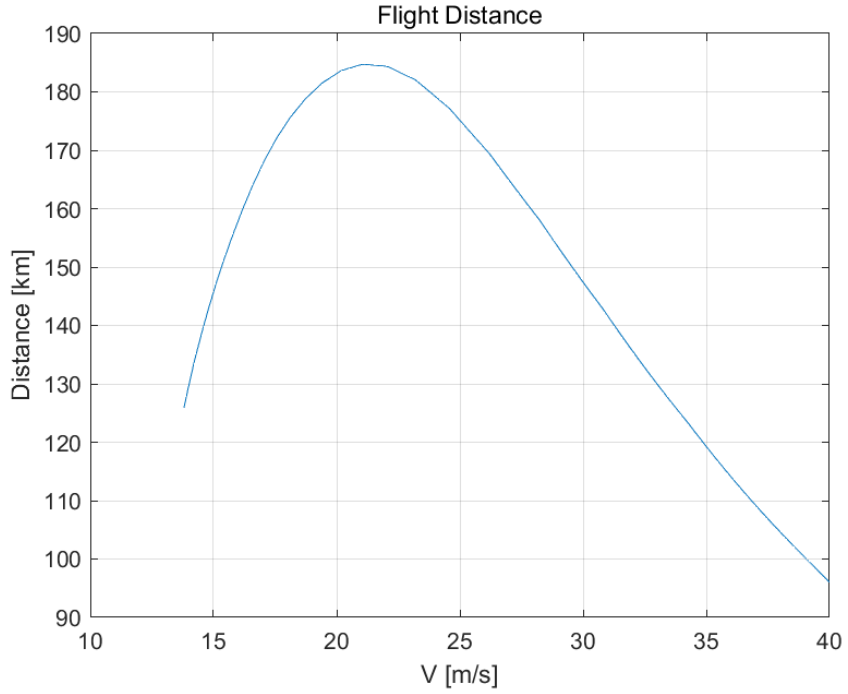

Figure 4.10: Maximal flight distance, which is the simple multiplication of flight time and speed. The maximum distance is achieved at around 21 $\mathrm{m\,s^{-1}}$, which is in fact higher the speed of lowest power consumption.

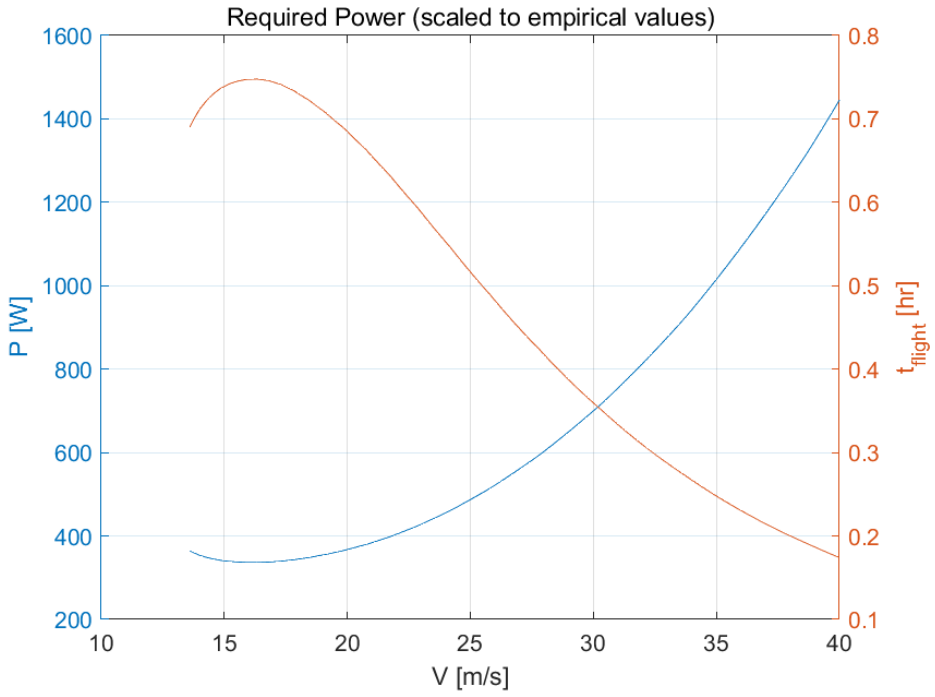

Figure 4.11: Same as Figure 4.9, but scaled to empirical values described in Table 4.1. The power consumption of the LiDAR system, see Section 6.2, has been included. Empirical power consumption is around four times higher than my calculations predict.

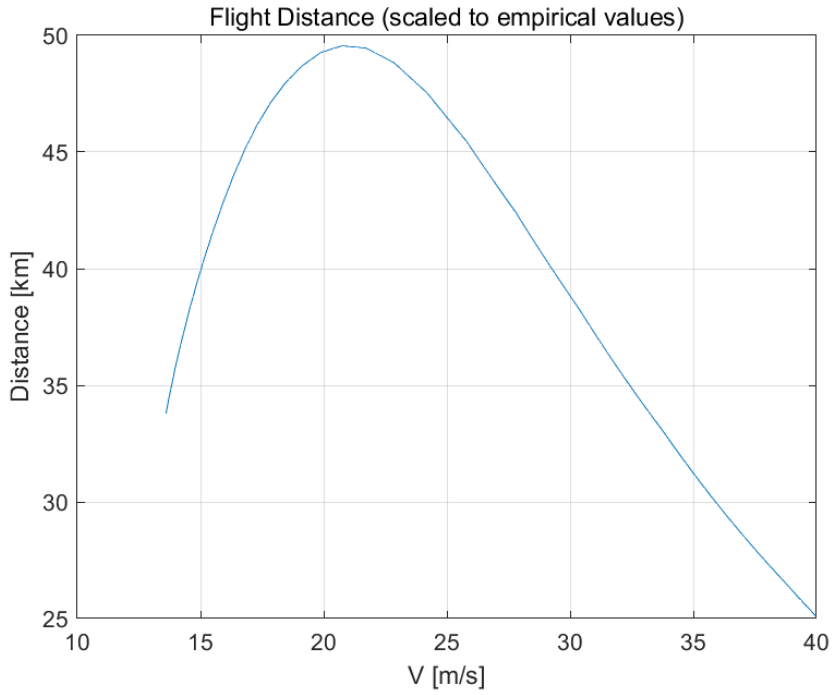

Figure 4.12: Distance achieved on one fuel tank based on power consumption in Figure 4.11. One fuel tank is sufficient only for a little under 50 km.

5

Soil Monitoring

5.1. Introduction

Soil is the basis of all life. Healthy soil produces healthy plants, which then feeds Earth's animals, including us. Soil health is determined by a variety factors, such as moisture retention, bulk density, pH, see Figure 5.1. The main indicator for soil health is the amount of soil organic carbon (**SOC**) stored in it[46]. A decrease in SOC not only affects fertility, but also water infiltration rate, soil biota[41], and may even cause erosion processes[11]. These processes degrade the soil which is self-reinforcing and releases carbon dioxide into the air[30]. In order to prevent such soil degradation, SOC should be maintained at or above 1.5–2% in the root zone[29].

Monitoring SOC levels is crucial for its maintenance and the optimal deployment of resources for replenishment. SOC can be measured in several ways, which have their own pros and cons:

- Laboratory measurement of soil samples. This is the most costly and slow process of all[46], as it involves the manual collection of samples from the field and sending them to a laboratory for analysis, where the samples are combusted and the emitted CO_2 measured. Equipment used in this method however is not limited by any weight constraints, and its results are thus the most accurate.
- Satellite imaging spectroscopy, i.e. taking color images from space. This method is very cost efficient as it can be employed over extremely large fields. However, this method can only measure proxies of soil content by analyzing vegetation reflectance in the various frequency bands. Naturally, it does not reach laboratory accuracy. Spatial resolution nowadays can be on the order of 10m (Landsat) down to 1m (WorldView-2). This is a lower resolution than what is possible using LiDAR.
- Airborne LiDAR. LiDAR is often employed for measuring distances, which is done by reflecting lasers off of objects, and measuring the time it takes for a signal to return. This approach is less rapid and cost efficient compared to satellite imagery, but more so compared to lab analysis. Advantages versus satellites are that there's no cloud interference, and the observation time and place are more flexible[27]. Although LiDAR systems are more costly than imaging sensors, their costs will likely come down[1] as they become more widely implemented[2], for example in self-driving cars.

In the next sections, we'll look at some methods and results from researchers who have employed satellite imaging or airborne LiDAR to measure soil carbon, with the ultimate goal of setting requirements for our own LiDAR drone.

5.2. Imagery and LiDAR

Measuring SOC using optical sensors from satellites or aircraft, also called remote sensing, is quite challenging compared to laboratory measurements. First, atmospheric absorption and the intrinsic solar spectrum

[1] `https://arstechnica.com/cars/2018/01/driving-around-without-a-driver-lidar-technology-explained/` Retrieved on 3 Dec 2018

[2] `https://www.grandviewresearch.com/industry-analysis/automotive-lidar-market?utm_source=abnewswire.com&utm_medium=referral&utm_campaign=abnewswire_26Nov&utm_content=Content` Retrieved on 3 Dec 2018.

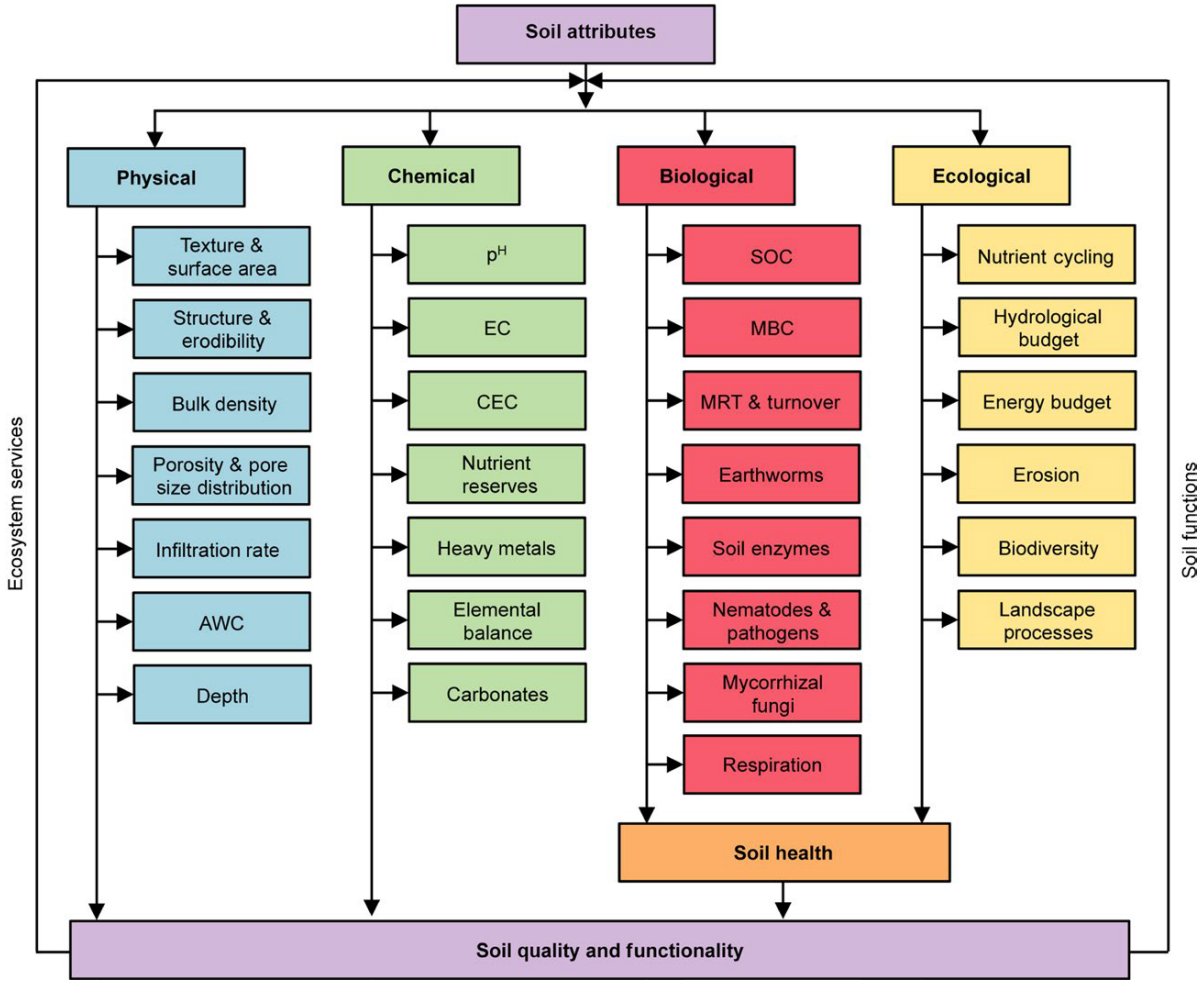

Figure 5.1: The plethora of soil parameters affecting its health. Taken from [29]

have to be accounted for. Then, the raw image data has to be corrected for geometry[11], at least when the landscape is not flat. After all this, there are still weather, climate and agriculture related processes such as soil crusting, vegetation, and crop residue[8] affecting the spectral response of the soil. Nevertheless, researchers all over the world are developing this method for its potential cost and time savings over laboratory measurements, with some success as we'll see below.

Broadly speaking, there are two ways to relate SOC to spectral response: by spectrometry/satellite imagery and by LiDAR. Some satellites can obtain data with spectral resolution of up to 10 nm, while other simply take images from space through several filters, usually red, green, blue, and (near) infrared, roughly approximating the spectrum of the landscape. LiDAR has the advantage of being able to measure elevation, even through dense forests. This data can be helpful for determining SOC[32].

A small literature search was performed with two goals mind: 1) find out the accuracy of these methods of estimating SOC, and 2) determine instrumental requirements of the sensors. All studies that I found use their own strategy of analyzing optical data to estimate SOC content. The general idea, however, is that SOC values of samples across an area are measured by taking the field samples to the laboratory. These values are then correlated with parameters (a.k.a. predictor variables) that are derived from the optical data. The variety of strategies is mainly due to the diversity of predictor variables. Resulting correlations vary and are shown in Table 5.1. In order to make sense of these results, the method of each research group will be described briefly in the following and in the same sequence as in the table. The first four of them uses satellite imagery, while the other three use LiDAR.

1. This study used a portable spectrometer AgriSpec to obtain in situ the SOC of 146 soil samples from their reflectance. A regression model was then fitted between this data and the spectral data from the Hyperion satellite. Table 5.1 gives the R^2 between the two sets of data.

2. This group first determined the regression equations between surface soil carbon concentration (**SSCC**) for 35 out of 55 data points and reflectance data from the SPOT-4 satellite. The remaining points were used to determine the accuracy. Afterwards, the correlation between SSCC and soil carbon stock (**SCS**) was determined. The table contains the RMSE for the difference between estimated SCS and measured SCS and the r value of the correlation between reflectance and SCS. I calculated this r value as the product of the r values between reflectance and SSCC and between SSCC and SCS. This is shown for volcanic ash in near infrared only, which had the highest correlation. The other soil types correlated similarly well in the red wavelength range.

3. Two intermediate parameters were considered here: bare soil index (**BSI**) and normalized difference vegetation index (**NDVI**). The BSI is an estimate of how bare the soil is and is a function of the red, green, blue, and near infrared colors. The NDVI is a measure of the amount of vegetation. See [12] for the formulae. Image data came from the LandSat satellite and the results in the table are for the correlation between SOC and both BSI and NDVI.

4. This research group used the most elaborate model involving many predictor variables for SOC. These are climate, lithology, relief, weathering and biota. Biota was remotely sensed using the LandSat satellite. The results in the table are without including biota. When biota is included, the accuracy improves by around 5%.

5. This group used an undisclosed LiDAR system to generate a digital elevation model (DEM). They included many environmental variables to predict SOC, some of which were not measured by LiDAR. The main influencers of SOC were precipitation, land use, soil type and terrain parameters, including elevation, slope gradient, SAGA wetness index, and multi-resolution index of valley bottom flatness (MrVBF).

6. The LiDAR system LiteMapper 5600[1] was employed in this study. Unfortunately for us, the authors do not specify the flight conditions. The direct correlation between reflected intensity and soil organic matter (SOM) is given in the table. SOM is the organic component in soil, which has SOC as the main component[18]. The ratio SOC/SOM is generally around 50%[26].

7. LiDAR (Leica ALS-40) is used in this study to determine the dimensions of trees (height and diameter at breast height). The aircraft flew at an altitude of 2.2km, and a speed of 80 knots. Using the LiDAR data only, the above ground biomass (**AGB**) was estimated and from the AGB the SOC. The AGB from LiDAR

was compared to laboratory measurements and this correlation is shown in the table. The largest SOC variations followed AGB variations, see their Discussion in [38].

Although the results shown in Table 5.1 are not comprehensive, some important points can be made:

- The most intuitive result is that in general, the deeper the soil depth, the more difficult it becomes to correlate the SOC with the optical data. In [2] specifically, the lowest R^2 (0.23) is for the deepest layer of soil at around 100cm, while the highest R^2 (0.63) is for the top layer at 0–5cm.
- In [35], SOC responded strongly in the red and near-infrared (**IR**) wavelength ranges. This is similar to the statement made by [32] (in their Introduction), that SOC correlates strongly with reflectance in the NIR–SWIR (short wavelength infrared) range with R^2 greater than 0.8.
- Comparing the two techniques of obtaining SOC estimates, satellite color images and LiDAR, the results are not significantly different. It's interesting that even though LiDAR does not contain color information, it reaches more or less the same accuracy. However, we should keep in mind that soil organic carbon is merely one component of soil organic matter, which is only one of the many soil properties that affect fertility. More complete spectral data is necessary to obtain information on those other properties[27].

The main conclusion from Table 5.1 is that it is possible to predict SOC using either simple images or LiDAR, and with an R^2 of up to around 0.7, at least in the studies shown. High resolution spectra, as in [19], are not necessary; simple color filters suffice as were used in [35], [12], and [46]. When it comes to LiDAR, the most important thing is that the intensity should be retrievable, which is what allowed [32] to obtain their results. The intensity or even pulse detection method is often not given, even though it may affect the accuracy of the measurements[1], since this knowledge is considered proprietary.

5.3. General LiDAR Requirement

For an estimate of LiDAR requirements for the estimate of SOC, I will focus on the studies in the last two rows in Table 5.1. As a reminder, the first uses reflected intensity (as a proxy for SOC), while the second uses the spatial resolution (to determine tree height and diameter, and thus SOC).

According to the specifications sheet[3] the LiteMapper-5600, which houses the RIEGL LMS-Q560 laser scanner, used by [32] consumes 120W. The frequency used by [38] was 52.9kHz.

The intensity required for a similar measurement, I_{req}, changes for a different flight altitude R, when neglecting atmospheric attenuation: the closer to the ground, the stronger the reflected signal. In the next chapter we will go much further into detail. As for the pulse frequency, a slower speed will allow us to use a lower frequency, when aiming for the same point density or spatial resolution. Using simple proportionalities we get:

$$I_{\text{req}} = I_0\left(\frac{R}{R_0}\right)^2 \tag{5.1}$$

$$f_{\text{p,req}} = f_{\text{p},0}\left(\frac{V}{V_0}\right) = 52.9\text{kHz}\,\frac{V}{41.2\text{m/s}} \tag{5.2}$$

Now, this calculation ignores noise. It's more useful to find an I_{req} that gives the same signal to noise. Flying at half the altitude, assuming a similar sensor size, would increase background intensity from reflected solar radiation by a factor of four, but the noise will increase only twice[4], according to Poisson noise. Hence $\sigma_I \propto 1/R$, and:

$$\frac{I_{\text{req}}}{\sigma_{I,R}} = \frac{I_0\left(\frac{R}{R_0}\right)^2}{\sigma_{I,R_0}} \tag{5.3}$$

$$\Rightarrow I_{\text{req}} = I_0\left(\frac{R}{R_0}\right)^2\frac{\sigma_{I,R}}{\sigma_{I,R_0}} = I_0\left(\frac{R}{R_0}\right)^2\frac{R_0}{R} = I_0\frac{R}{R_0} = 120\text{W}\frac{R}{2.2\text{km}} \tag{5.4}$$

[3] `http://www.riegl.com/uploads/tx_pxpriegldownloads/10_DataSheet_Q560_20-09-2010_01.pdf`, Retrieved on 4 Dec 2018

[4] There are other noise factors, one in the LiDAR signal itself and another in the dark current. But these are not significant during daytime, compared to the solar radiation background noise[21].

Table 5.1: An overview of several studies on SOC measurements by remote sensing. The mentioned soil types are oversimplified, and the respective papers should be consulted for more complete descriptions of the soil. The Spectral Range column describes either the full range with resolution in brackets or the individual range of the bands. SR stands for Spatial Resolution, which is the spatial resolution of the satellite. The Root Mean Square Error (**RMSE**) column contains the relative error, i.e. error divided by measured value, and in square brackets the absolute value if this is mentioned in the source. The R^2 values describe the correlation between the optical measurement and SOC content, see also text for the interpretation of these values.

				Spectroscopy				
	Location, Country, Year of publication, Area size	Soil or Forest Type or vegetation	Soil Depth	Spectral Range (Resolution)	SR	RMSE	R^2	Source
			[cm]	[nm]	[m]	[Mg C/ha]		
1	Narrabri, Australia, 2008, –	Vertisol	0–10	400–2500(10)	30	73%	0.51	[19]
2	Tokachi District, Japan, 2011, 240 km^2	alluvial deposits and volcanic ash	0–30	500–590, 610–680, 780–890, 1580-1750	20	<20% [19.5]	0.76	[35]
3	Medinipur Block, India, 2017, 323.6 km^2	Laterite soil	0–20	450–520, 520–600, 630–690, 760–900	30	1.11(?)	0.71	[12]
4	New South Wales, Australia, 2018, 233 877 km^2	grasslands, shrubs, scattered trees	0–30	same as 3	same as 3	[9.16]	0.44	[46]
				LiDAR				
				Wavelength [nm]	Pulse rate and length [kHz], [ns]			
5	Denmark, 2014, 43 000 km^2	coarse sandy to heavy clay	0–100				0.23–0.63	[2]
6	Liangshui National Nature Reserve, China, 2016, 40 km^2	Korean pine forest	0–100	1556	150, 3.5		0.64	[32]
7	Chitwan, Nepal, 2017, 6.6 km^2	Sal forests, mixed forests	0–20		52.9	31%	0.69	[38]

The altitude was not given by the authors, so I assumed 2.2 km, which was used in [38]. As an example, we can use an altitude of 50m, and speed of 25m/s, then

$$I_{\text{req}} = 2.73\text{W},\ f_{\text{p,req}} = 32\text{kHz} \tag{5.5}$$

It's possible to fly (s)lower to make these requirements easier to achieve.

These requirements can be regarded as upper limits, as they are based on the specifications of a real LiDAR system that was employed, and so using a higher intensity or frequency should not be necessary. Note that only one of the requirements has to be satisfied, since the two were used in two separate methods of estimating SOC. It is difficult to find a small LiDAR system which allows the retrieval of intensity information, so we will focus on the second requirement in the next sections. The second requirements is quite high for a small LiDAR system, but we can find a lower requirement for the pulse frequency by determining what point density is necessary for accurately determining tree height and diameter of individual trees. In the following, we will focus on the LiDAR specifications required to perform a measurement similar to the study by [38] (row 7 in Table 5.1), which is based on tree height.

5.4. Point Density Requirement

With a point density of 4–14 per m^2, [24] found a determination coefficient of R^2 = 0.94, for mature forest stands, between heights measured by LiDAR and data from the National Forest Inventory in Australia, though for young forest stands this drops to R^2 = 0.53, possibly due to the closer distances between young trees. [10] obtained a lower coefficient R^2 = 0.65, with a mean that's 3.73m higher for LiDAR measurements compared to field measurements. The author ascribed the errors to several causes, one of which was the difficulty to identify individual trees. It should be noted that their LiDAR point density was 2.4 points/m^2. There is one study that uses a resolution of 1m [45], and found a high coefficient between LiDAR measured and manually measured heights of R^2=0.93. but gives no measurement errors. [4] obtained a mean error and standard deviation of LiDAR based heights compared to field measurements of -0.73 ± 0.43m, using a density of 6 points/m^2. They also gave an overview of previous measurements, which I have plotted in Figure 5.2.

In conclusion, when measuring tree height using LiDAR it's crucial to be able to identify individual trees: the distance between LiDAR measurements points should be small, while the distance between the trees themselves should be large. From Figure 5.2, we can conclude that a point density of more than 5 points/m^2 does not improve accuracy. Hence, for simplicity, we will use 5 points/m^2 as a minimal requirement for accurate soil carbon measurements (through tree heights) using the Delftacopter.

One last point to be made here is that all of the studies above use either LiDAR mounted on an aircraft or on a helicopter. By mounting it on a drone, there may be additional measurements errors due to the smaller total weight, and hence lower inertia of the vehicle.

Now, suppose we scan a rectangular area A, with length and width L and W, using a LiDAR system with F as pulse frequency. Then the point density (per unit area) is given by[6]:

$$d = \frac{FnT_{\text{s}}}{A} \tag{5.6}$$

with n the number of strips required to cover the area, which depends on the desired overlap and swath width, see [6] for details. $T_{\text{s}} = L/V$ is the flying time per strip, and this is where the flight speed, V, comes in. A higher speed leads to a lower point density, all else remaining equal. In the following chapter, we will model the point density for a selected LiDAR system.

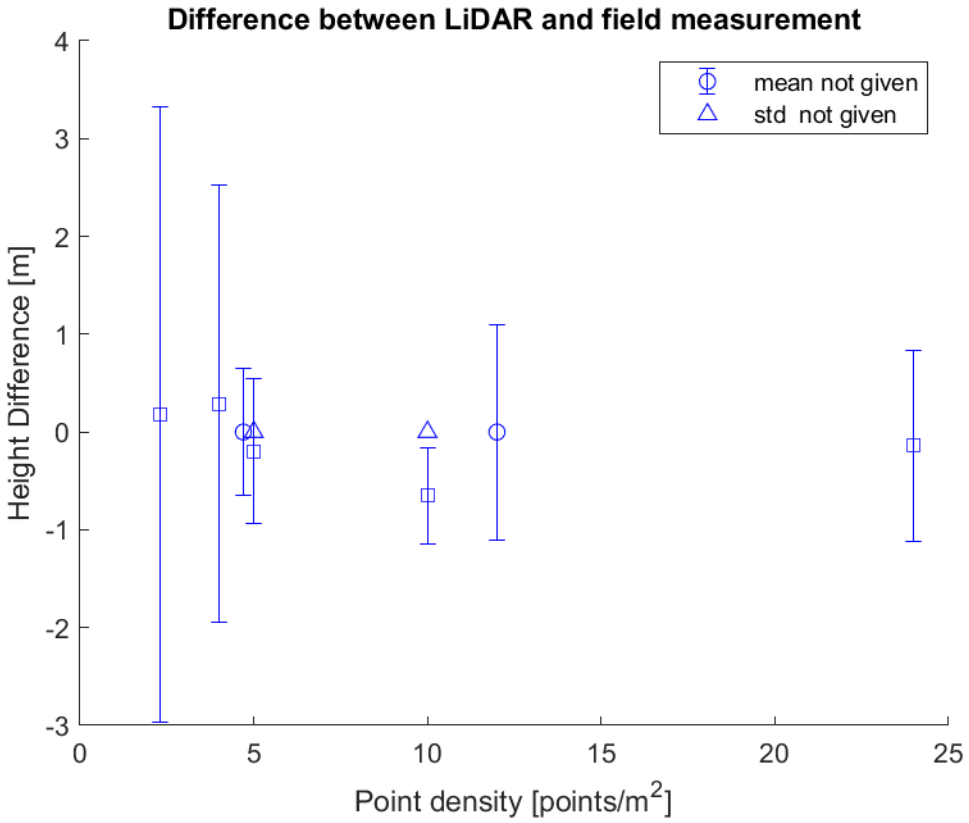

Figure 5.2: Point density of LiDAR measurements versus obtained accuracy of tree height. Trees were measured from the ground and from the air using LiDAR. The difference between the two is on the y-axis. For some of the data points either the mean or the standard deviation from the mean was not given.

6

LiDAR range

6.1. Introduction

In the previous chapter, we have discussed the requirements for the LiDAR system. In this chapter, we choose and analyze one that fits those requirements. An attempt was made to estimate the range using radiative transfer equations, including atmospheric absorption, scattering and reflection by vegetation. The data density that the system can achieve was modeled for different flight speeds and rotation rates, using the range specified by the manufacturer.

6.2. LiDAR Selection

The LiDAR system that I chose is the Puck LITE from Velodyne[1], which weighs 590 g and has a diameter of 103 mm. For it to function properly, the interface box needs to be added. I could not find its weight, so I assumed a weight of 200 g, which is based on the size of the device and weight of circuit boards.

There are 16 lasers inside the device firing at a rate of 18 kHz. The total pulse frequency of 289 kHz surpasses the requirements set in the previous chapter. In the following two subsections, the performance of this LiDAR system is estimated.

6.3. LiDAR Range Estimation

The practical range of the LiDAR system was estimated through radiative transfer calculations. The strategy was to calculate the strength of the LiDAR signal and compare this with all noise sources.

A laser beam that is sent out by the LiDAR emitter will go through three events that diminishes its intensity. First, the atmosphere partially extinguishes the light, while it spreads out geometrically across space. When these photons touch an object, some will be lost in the material as a small amount of heat, while the remaining photons are scattered back in random directions. Lastly, the returning portion of light will experience the same dilution as in the first step, before returning via a filter to the detector.

As for the background radiation coming from the Sun, this has been obtained from SMARTS (Simple Model of the Atmospheric Radiative Transfer of Sunshine). The background radiation hits an object and goes through the same processes as described above. Calculations for these processes will be described in the following subsections.

6.3.1 Background radiation

A beam of light at wavelength λ with an intensity $I(\lambda)$ experiences extinction by absorption and scattering. If we assume that the beam retains a constant diameter, then its intensity along a path x can be described by the Lambert–Beer law:

$$\frac{\mathrm{d}I(x,\lambda)}{\mathrm{d}x} = -b(x,\lambda)\,I(x,\lambda) \tag{6.1}$$

[1] https://www.velodynelidar.com/vlp-16-lite.html

Location	Humidity [%]	Water vapor density [g/m^3]	Temperature [°C]
Amazon rain forest (winter)	77%	13.32	20
Amazon rain forest (summer)	88%	33.59	34
Netherlands (winter)	86%	4.34	0.5
Netherlands (summer)	80%	15.76	22.1

Table 6.1: Water vapor density in two geographic locations and two seasons.

where b is the extinction coefficient, which is the sum of the absorption and scattering coefficients. The intensity as a function of distance is therefore

$$I(x,\lambda) = I(0,\lambda)\cdot e^{-bx} \tag{6.2}$$

The absorption and scattering coefficients of air will be provided by literature. We will limit the analysis to wavelengths close to the laser wavelength of 903 nm, namely 800–1000 nm. Light at other wavelengths will be blocked to a large extent by the near-IR filter.

6.3.2 Absorption and scattering by air

According to figure 4.9 in [42], the most significant absorber in our wavelength range is water vapor. Since the amount of water vapor can vary by geographic location and season, I have selected four extreme, yet real conditions on Earth in order to capture the range of this variation[2], see Table 6.1.

The water vapor density was calculated as the multiplication of humidity and saturated water vapor density at a given temperature, obtained from HyperPhysics[3]. You can see that the amount of water vapor can vary by an order of magnitude.

The absorption cross section of water can be found on the HITRAN[20] website[4]. Cross sections between wavenumbers 9703.344294 – 12379.372242 cm^{-1} (807.8 – 1030.6 nm) and between 11376.529824 – 13034.654224 cm^{-1} (767.2 – 879 nm) were used, corresponding roughly to wavelengths of 800 – 1000 nm. The data is plotted in Figure 6.1.

The transmittance and intensity can then be calculated as

$$T(x,\lambda) = \exp\Big(-\frac{\sigma_{\text{abs}}(\lambda)\rho_{\text{vap}}}{M_{\text{H}_2\text{O}}N_A}x\Big) \tag{6.3}$$

$$I(x,\lambda) = I_0(\lambda)T(x,\lambda) \tag{6.4}$$

with x the path length, σ_{abs} the aforementioned absorption cross section, ρ_{vap} is the water vapor density in g cm^{-1}, $M_{\text{H}_2\text{O}}$ the molecular weight of water in g mol^{-1}. The following scattering calculations were based on [13], which incorporates the largest constituents of air, namely nitrogen and oxygen, but also conveniently the CO_2 concentration. Their formula for the scattering cross section is

$$\sigma_{\text{scat}} = \frac{24\pi^3(n^2-1)^2}{\lambda^4 N_s^2(n^2+2)^2}F(\text{air},\text{CO}_2) \tag{6.5}$$

with N_s the number density in molecules per cm^3, λ the wavelength in cm, $n = n_{\text{CO}_2}$ the refractive index of air at a certain CO_2 concentration, and $F(\text{air},\text{CO}_2)$ the depolarization factor. The refractive index is calculated with the following equations[13]

$$n_{300} - 1\cdot 10^8 = 8060.51 + \frac{2480990}{132.274-\lambda^{-2}} + \frac{17455.7}{39.32957-\lambda^{-2}} \tag{6.6}$$

$$\frac{n_{\text{CO}_2}-1}{n_{300}-1} = 1 + 0.54(\text{CO}_2 - 0.0003) \tag{6.7}$$

[2]Data from `http://www.thesustainabilitycouncil.org/tropical-rainforest-biome.html`, and `https://www.weather-atlas.com/en/netherlands/amsterdam-climate`

[3]`http://hyperphysics.phy-astr.gsu.edu/hbase/Kinetic/watvap.html`

[4]`http://hitran.iao.ru/`

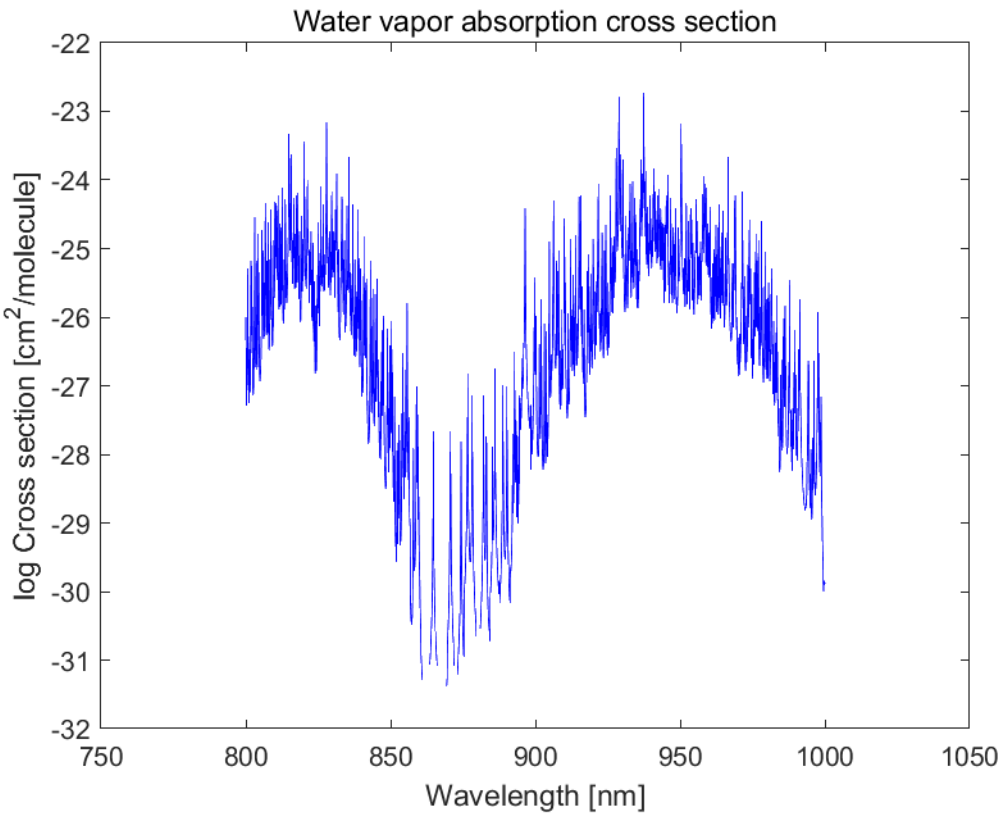

Figure 6.1: Cross section of water vapor between 800 and 1000 nm

where n_{300} is the refractive index of air at 300 ppm CO_2. λ is the wavelength in µm. The depolarization factors[13] are

$$F(\text{air}, CO_2) = \frac{78.084 F_{N_2} + 20.946 F_{O_2} + 0.934 + CO_2 \cdot 1.15}{78.084 + 20.946 + 0.934 + CO_2} \tag{6.8}$$

$$F_{N_2} = 1.034 + \frac{3.17 \cdot 10^{-4}}{\lambda^2} \tag{6.9}$$

$$F_{O_2} = 1.096 + \frac{1.385 \cdot 10^{-3}}{\lambda^2 + 1.448 \cdot 10^{-3} * (\lambda)^4}; \tag{6.10}$$

where CO_2 is now the amount of CO_2 in volume percent, that is 0.036 for 360 ppm. In these formulas it is assumed that the parts per volume of other constituents of air remain constant for an increased CO_2 concentration, which is mathematically false. But for our purposes, the resulting loss in accuracy is negligible.

The solar spectrum as obtained from SMARTS is plotted in Figure 6.2. The maximum altitude of the Sun during summer and winter were taken from the Sun path chart program[5] by the University of Oregon. In the following sections, the amount of radiation is calculated as it is reflected, absorbed and scattered, and as it enters in the detector.

6.3.3 Albedo

The reflectance of the vegetation determines what part of the background radiation and LiDAR signal comes back, and varies by species. Figure 6.3 shows the albedo of a variety of plants and trees which were provided by the SMARTS program. As can be expected, the spectra look very similar. They differ mostly on the average albedo. For this reason, I have selected three based on their overall albedo: Green grass, Deciduous oak tree, and Ponderosa pine tree. In Figure 6.4, you can see the effect of albedo on the reflected solar spectrum. The LiDAR signal has been multiplied as well by the albedo value at its wavelength.

[5] `http://solardat.uoregon.edu/SunChartProgram.html`

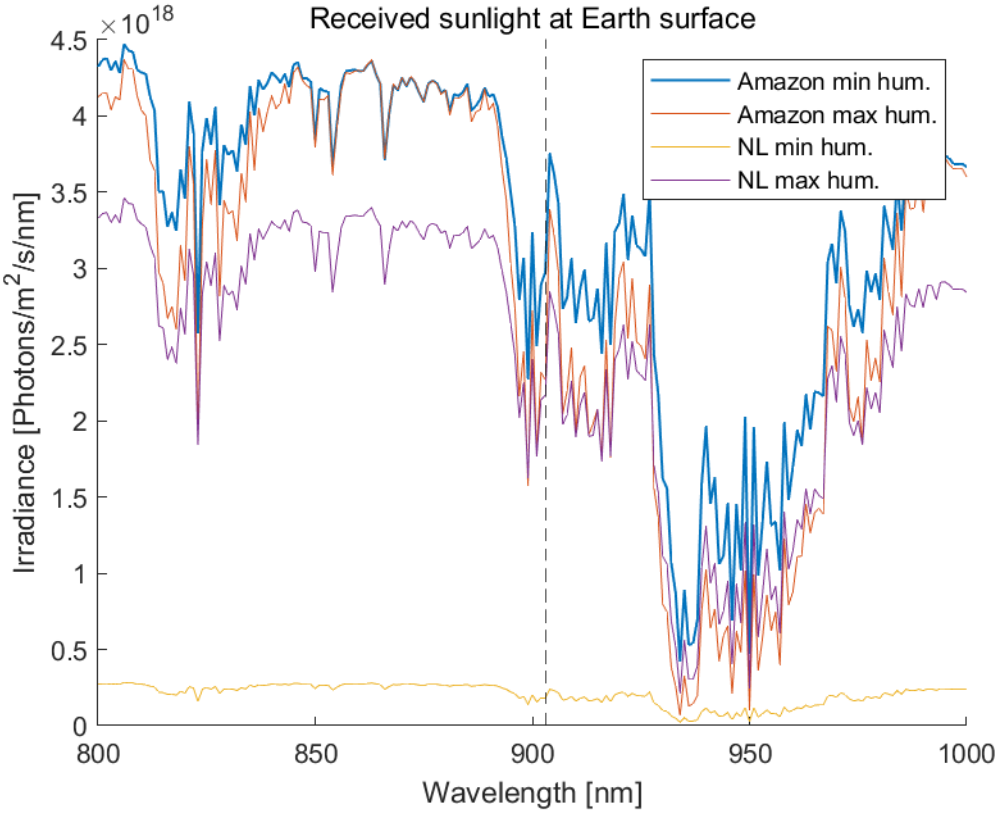

Figure 6.2: Solar spectrum for different humidities and locations. These are all corrected for the maximum altitude of the Sun. During winter in the Netherlands, the Sun reaches at most an altitude of 15°

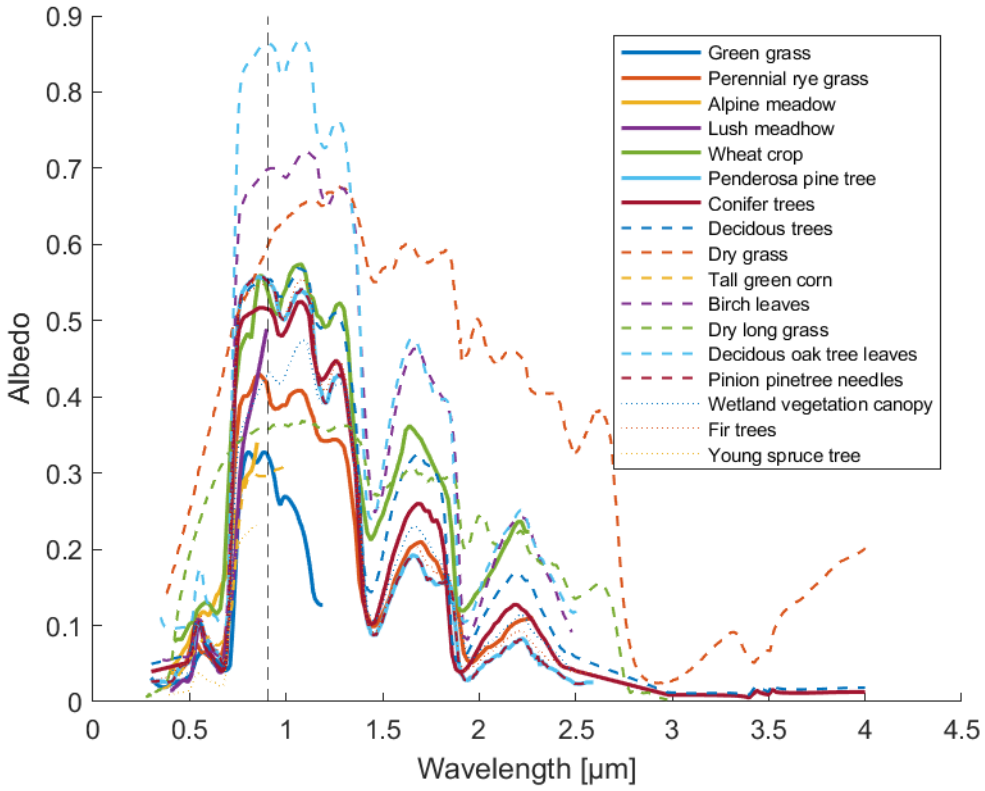

Figure 6.3: Albedo of different grasses and trees. The black striped vertical line indicates the wavelength of the LiDAR laser.

6.3.4 Return path

After being reflected by vegetation, the radiation is again absorbed and scattered by the air. So we need to calculate the radiative transfer as was outlined in Section 6.3. From my calculations based on formulae outlined in Section 6.3.2, absorption and scattering are both only about 0.1% per 100 m.

6.3.5 IR filter

A near-IR filter is used to isolate the LiDAR signal from the background noise. Since it was difficult to find full specifications of the Velodyne Puck-LITE system, I searched for a filter that would fulfill this purpose.

The 905 nm filter by Salvo Technologies[6] seems to fit well. In Figure 6.5, the effect of this filter is shown. Wavelengths outside of 800–100 nm range have been neglected.

Due to computational reasons[7], the filter was applied immediately to the background radiation and also the LiDAR signal. This should not be a problem, since the filter is a simple multiplication, which is a commutative operation.

6.3.6 Geometry

Of course, vegetation does not act as a mirror. The light is scattered in random directions upon hitting the surface of a leaf. I have assumed these leaves to be Lambertian scatterers, and that they are lying flat on the ground, so that the angle of incidence is simply the angle at the ground.

The field of view (**FOV**) of the detector should be small so that, similar to the purpose of the filter, the LiDAR signal is isolated from the background noise. The FOV is determined by the focal length of the lens and the size of the photodiode. Avalanche photodiodes are designed for high sensitivity applications such as the

[6] `https://opticalfiltershop.com/shop/bandpass-filter/nir-bandpass-filter-905nm-fwhm-50nm/`

[7] My radiative transfer calculations were done for a large amount of angles between the drone and the ground, i.e. θ in Figure 6.6. In order to save memory space, the background solar spectrum is integrated over wavelength for every angle, after which it is impossible to apply the filter. Therefore the filter has to be applied before this process.

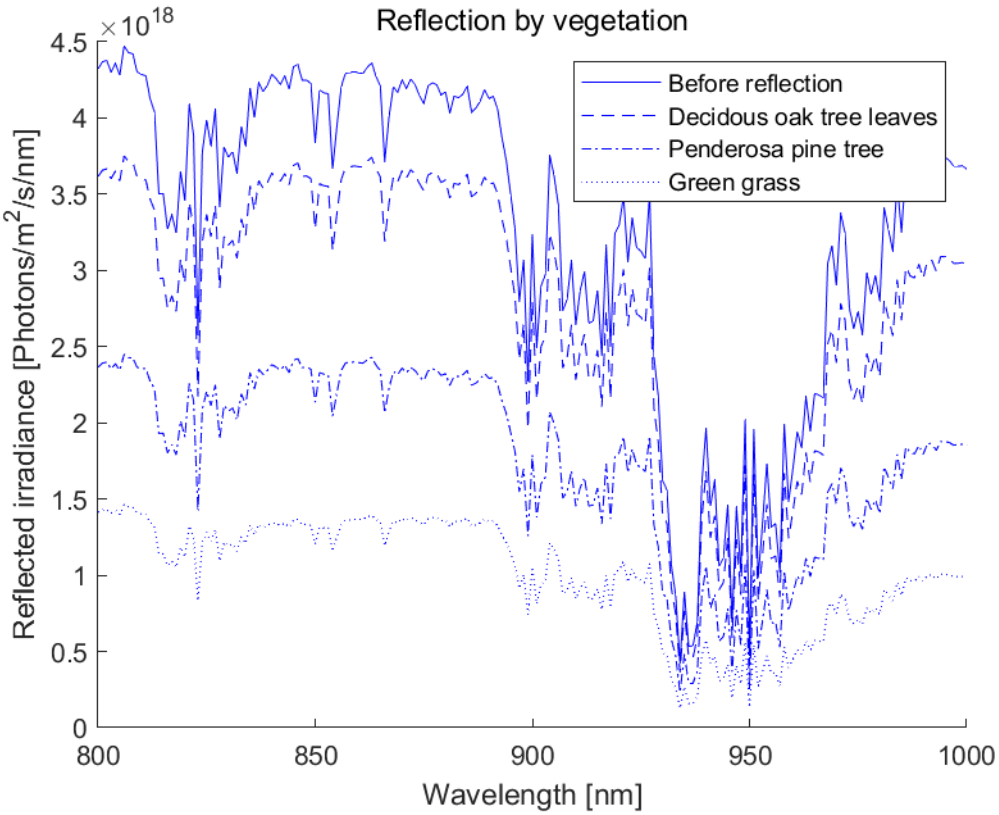

Figure 6.4: Reflected solar spectrum for different albedo profiles in the Amazon rain forest in the winter. The mentioned trees may or may not actually grow in this climate.

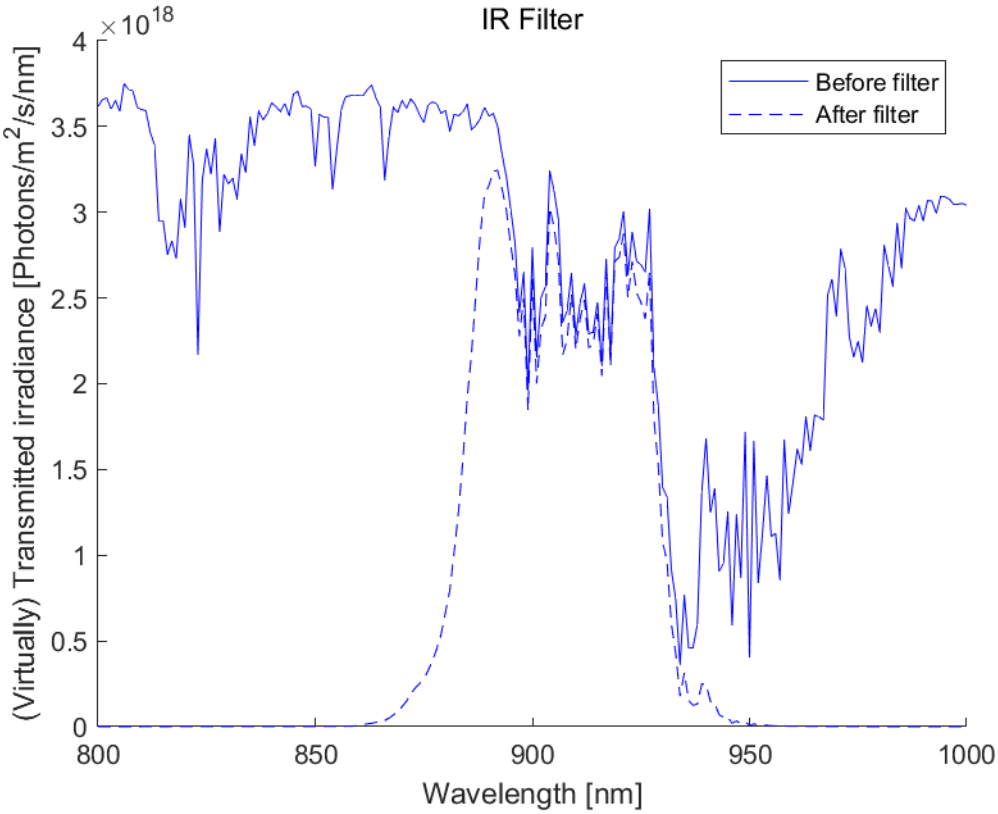

Figure 6.5: Solar spectrum before and after applying the near-IR filter.

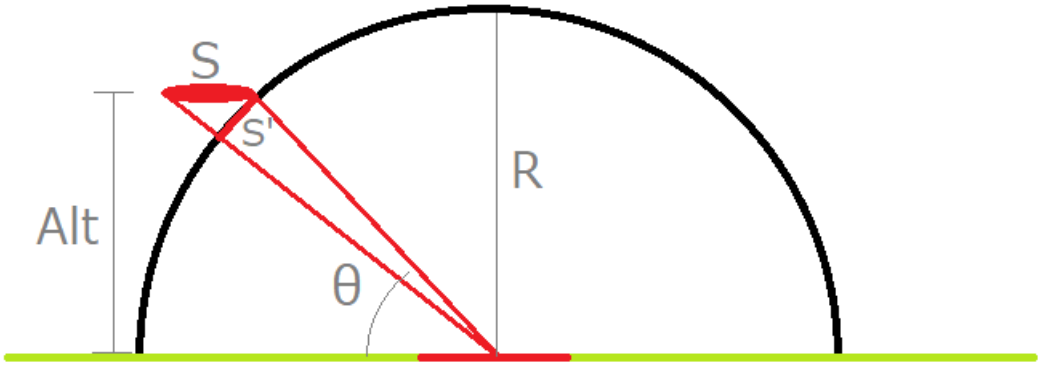

Figure 6.6: Sketch of a drone LiDAR measurement. The LiDAR signal is shot at some angle θ and hits the ground, and is partially reflected back to the detector. The detector sees a larger area, indicated by the red surface, than the dot illuminated by the laser on the ground.

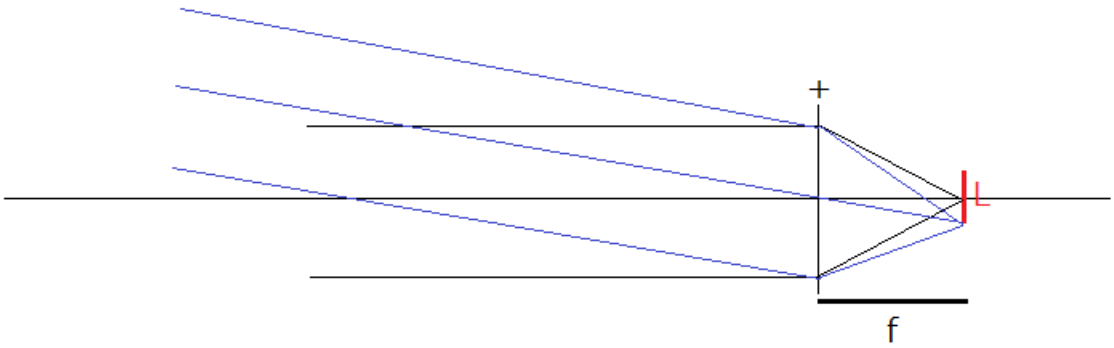

Figure 6.7: Schematic drawing of field of view of the LiDAR detector.

detection of a LiDAR signal at large distances. I have chosen the S3884 avalanche photodiode by Hamamatsu[8] which works in our wavelength range. This photodiode has a diameter of 1.5 mm. The focal point is assumed to be 2 cm keeping in mind the dimensions of the LiDAR emitter. The size of the lens is assumed to be 3 cm in diameter.

By constructing the light rays in a schematic drawing as in Figure 6.7, we can find the field of view as simply twice the angle between the blue rays on the left of the lens with the horizontal axis:

$$\mathrm{FOV} = 2 \cdot \arctan \frac{L}{2f} \tag{6.11}$$

where L is the total length of the photodiode, and f the focal length. For the quantities given above, the FOV is 4.3°, or about 1000 times the angular size of the laser beam.

The background radiation has to be multiplied by the area on the ground that the detector can see. For simplicity I assumed this area to be a trapezoid on the ground, calculated as the multiplication of length and width:

$$L_{\mathrm{trap}} = \tan(\mathrm{FOV}) \frac{\mathrm{Alt}}{\sin(\theta)} \tag{6.12}$$

$$W_{\mathrm{trap}} = \frac{\mathrm{Alt}}{\tan(\theta - \mathrm{FOV}/2)} - \frac{\mathrm{Alt}}{\tan(\theta + \mathrm{FOV}/2)} \tag{6.13}$$

$$S_{\mathrm{trap}} = L_{\mathrm{trap}} \times W_{\mathrm{trap}} \tag{6.14}$$

The part of the radiation that actually reaches the detector is proportional to the projection of the detector surface onto the sphere with radius R, or S' in Figure 6.6. This can be approximated as

$$S' = S \sin(\theta) \tag{6.15}$$

The fraction is then

$$\frac{S'}{S_{\mathrm{sphere}}} = \frac{S * \sin(\theta)}{2\pi R^2} \tag{6.16}$$

$$R = \frac{\mathrm{Alt}}{\theta} \tag{6.17}$$

6.3.7 LiDAR signal strength

The power consumption of the Velodyne Puck LITE is 8 W. The fraction that is converted from this power to photons, $\eta_{P,\mathrm{phot}}$ is not given. From an exploration of literature[14][3], the efficiencies ranges from a few percent to 58%. I assumed therefore an efficiency of 25%. The amount of photons per laser per second, N_{phot} is then the laser power output, $\eta_{P,\mathrm{phot}} P$, divided by the energy per photon, E_λ, at $\lambda = 905\,\mathrm{nm}$, divided over 16

[8] https://www.hamamatsu.com/eu/en/product/optical-sensors/apd/si-apd/index.html

	Amazon min.	Amazon max.	Netherlands min.	Netherlands max.
Deciduous oak tree leaves	1230.83	1230.83	1911.82	1325.05
Ponderosa pine tree	1149.19	1149.19	1721.06	1230.83
Green grass	1077.79	1077.79	1565.01	1149.19

Table 6.2: Range estimates in meters for the LiDAR system in different humidity levels and vegetation. min. refers to winter with minimal humidity, while max. refers to summer with maximal humidity.

lasers:

$$N_{\text{phot}} = \frac{\eta_{P,\text{phot}} P}{16 \cdot E_\lambda} = \frac{0.25 \cdot P}{16 \cdot \frac{hc}{\lambda}} \tag{6.18}$$

$$= 5.682 \times 10^{17}\,\text{s}^{-1} \tag{6.19}$$

with h the Planck constant, and c the speed of light.

6.3.8 Signal and Noise

In our setup, the signal is that of the LiDAR laser beam coming from the emitter, bouncing off of vegetation, and into the detector. The noise source is the background solar spectrum reflected and scattered by vegetation into the detector. The noise source can be subtracted to a large extent, but noise will remain. Assuming Poisson noise, the noise is the square root of the radiation. Other noise terms include dark current noise, and Poisson noise in the LiDAR signal, but these are negligible.

I have considered the signal to be detectable, if the signal to noise ratio is larger than three. At a given angle with the ground, the combination of radiative transfer and geometry will determine the signal to noise as described in the previous sections.

6.3.9 Range results

Unfortunately, the range estimation I've obtained seem too large. They are summarized in Table 6.2. We can however see that the environmental conditions can have a large impact on the range, if the numbers are relatively correct. During the winter in the Netherlands (minimal humidity), the range is around 50% higher than during summer (maximal humidity). This has to do with the fact that the Sun is not as bright during the winter, which reduces the background radiation significantly. Humidity levels have a negligible effect on the range (Section 6.3.4).

In Figure 6.8, you can see the radiation intensity as the LiDAR signal and background go through the atmosphere. The largest reduction is due to the fact that the detector is very small compared to where the radiation is scattered. We can conclude that scattering and absorption by air has a negligible effect on the range, while albedo may have a small effect of around 10%.

6.4. Point Density Simulation

In the previous sections, an attempt was made to estimate the LiDAR range under various conditions. Since that attempt was not fruitful, I will now continue with a range of 100 m as stated in the specifications.

As argued in Section 5.4, the minimal required point density is 5 points per square meter, or $5\,\text{m}^2$. This resolution, along with the maximum range of 100 meters, will limit the area coverage.

A simple way of analyzing the point density is to simulate the points. As a reminder, the LiDAR system consists of 16 lasers, which simultaneously fire every 55.296 µs. The LiDAR system is placed such that the rotational axis is along the flight direction (y-direction), so that it scans along the perpendicular direction (x-direction). A sizable part of the light bundles will simply be sent into the air as the drone flies over the ground. In case the drone is sent below the tree canopy, it will of course collect more data points.

In Figure 6.9, you can see the simulated laser dots for one LiDAR system revolution on a flat surface for a certain LiDAR rotation rate, flight speed, and altitude. The drone is positioned at $x = 0$. The angles between the lasers create a flaring effect at x-positions further away from $x = 0$. For multiple revolutions, seen in Figure 6.10, quite an astonishing pattern emerges with areas of lower point density than others. In reality this pattern will likely disappear due to the instabilities of the drone and errors in the inertial measurement unit.

The point density can now be obtained by simply counting the number of points in each square meter. The result is shown in Figure 6.11. The horizontal range of the LiDAR system at these flight conditions is then

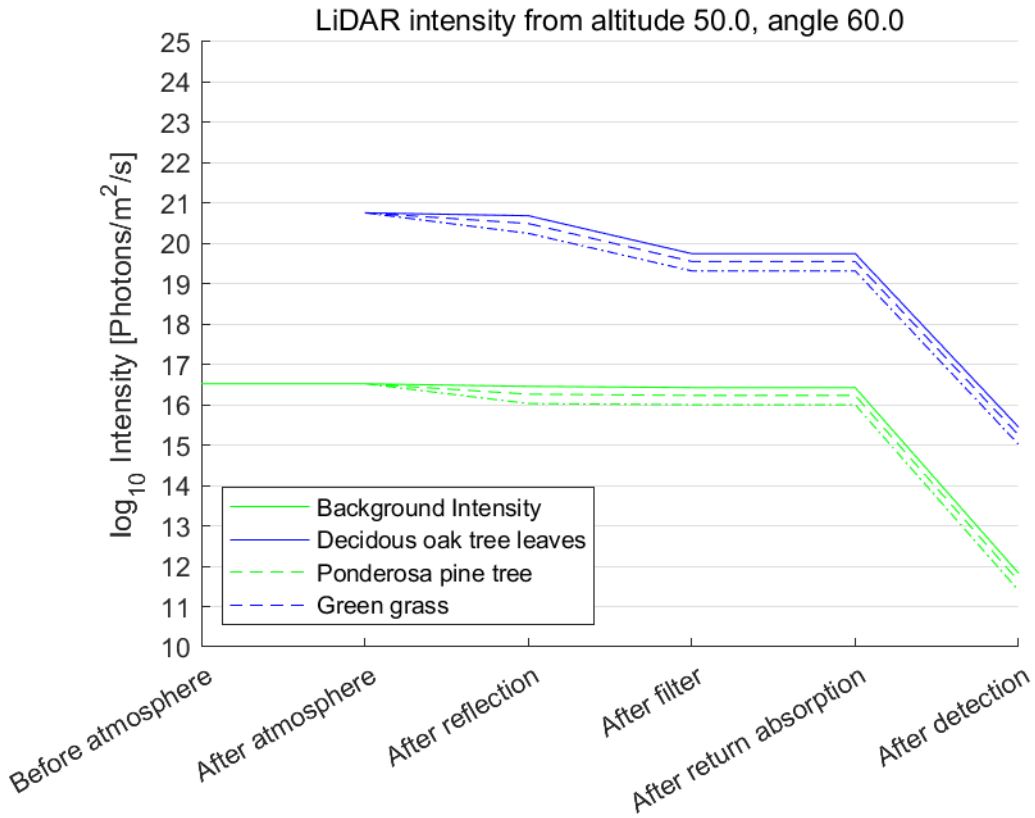

Figure 6.8: Radiation intensity of LiDAR signal and background radiation after different events. The background radiation was obtained from SMARTS, which gives you the solar spectrum as received on the ground. The LiDAR goes through atmospheric absorption, described in Section 6.3.2. After hitting the vegetation on the ground, the light is reflected back. The filter in the detector allows only wavelengths near the laser wavelength, and therefore only affects the background radiation. As the light travels from the vegetation to the detector, it is again partially absorbed and scattered by the atmosphere. This only leads to a 0.1% drop in intensity per 100 meters, so it is not noticeable in this plot. The detector at the end of the journey catches a very small fraction of all the light, see also Section 6.3.6.

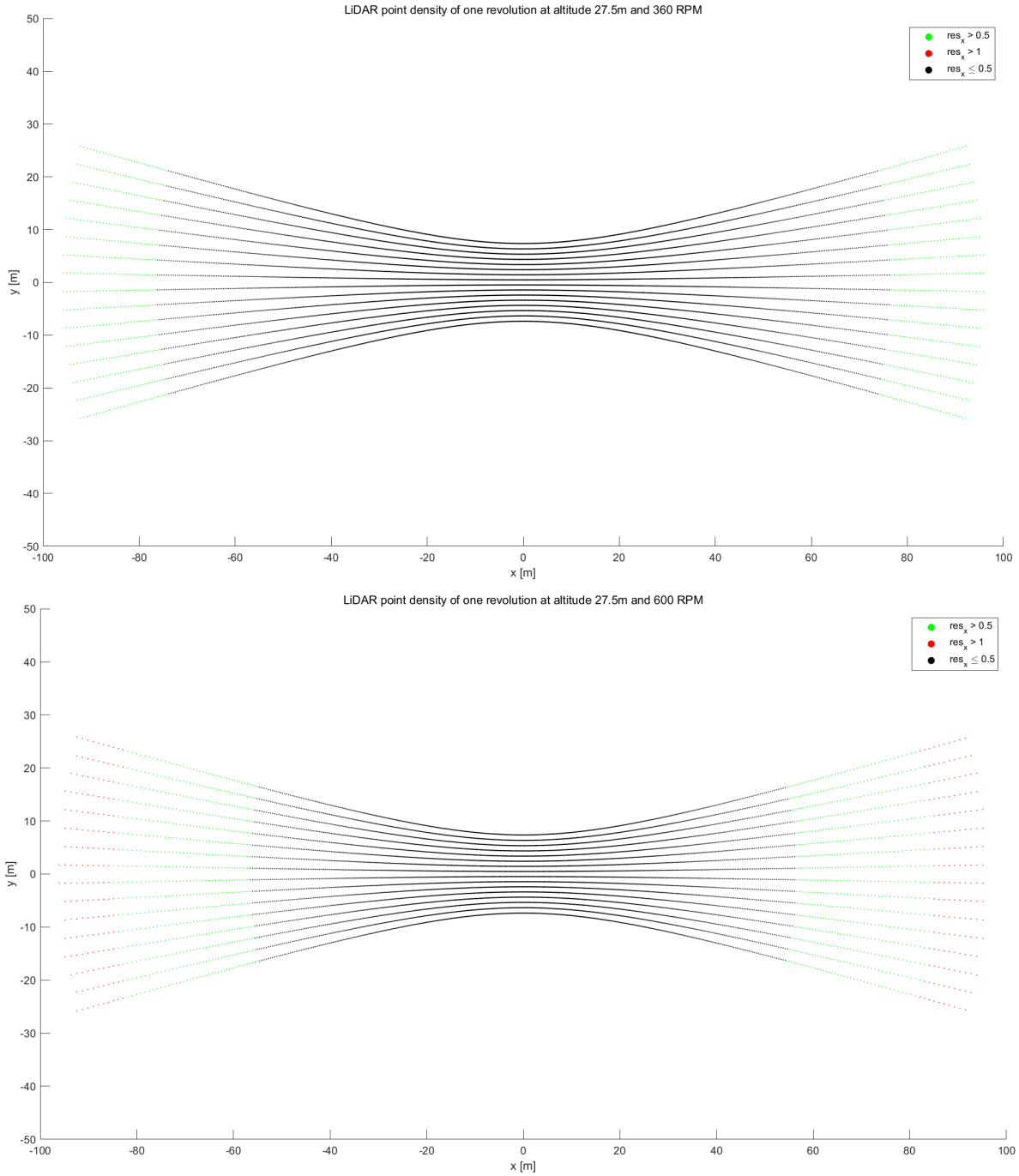

Figure 6.9: Simulated LiDAR measurement of one revolution at 6 Hz (top) and 10 Hz (bottom) rotation rate, an altitude of 27.5 m and flight speed of 20 $m\,s^{-1}$ in the y-direction. The simulation is done for a flat surface. Every dot represents a point which is illuminated by the lasers. The dots are not to scale. For green dots, the point density in the x direction is less than 5 m^2 but more than 2.5 m^2. For red dots, the point density in the x direction is less than 2.5 m^2.

calculated as the number of the 1x1 m bins in the x-direction which have a point density higher than 5 m^2 plus half the bins with point density between 5 m and 2.5 m.

The figure was cut off at 10 points per square meter. However, the point density shoots up to 80 /m^2 at the $x = 0$ m then rapidly drops off to around 25 /m^2 at around $x = 25$ m. If it were possible to redistribute these points, the homogeneity of the data points could be improved or the range could be extended, at least when only considering point density constraints. Redistributing these points is not very practical for a rotating LiDAR system, as it would require continuous rapid accelerations. A solid state LiDAR sensor, which contains no moving parts but changes its laser direction by wave interference, would be better suited for this purpose.

6.5. Area Coverage

Having obtained the horizontal range, the area per second covered with sufficient point density by the LiDAR system is now simply the horizontal range multiplied by the velocity. The velocity was chosen to be 20 $m\,s^{-1}$, as this is the speed which can reach the longest distance, see Section 4.4.4. The analysis as shown in Section 6.4 was performed for a range of altitudes and rotation rates, and is shown in Figure 6.12.

The optimal configuration for maximum area coverage for a flight speed of 20 $m\,s^{-1}$ is an altitude of 27.5 m and rotation rate of 10 Hz, which is enables a coverage of around 3740 m^2/s.

In Figure 6.13, the results for higher flight speeds is shown, which are based on the exact same calculations. We will refer back to these two figures in the next chapter.

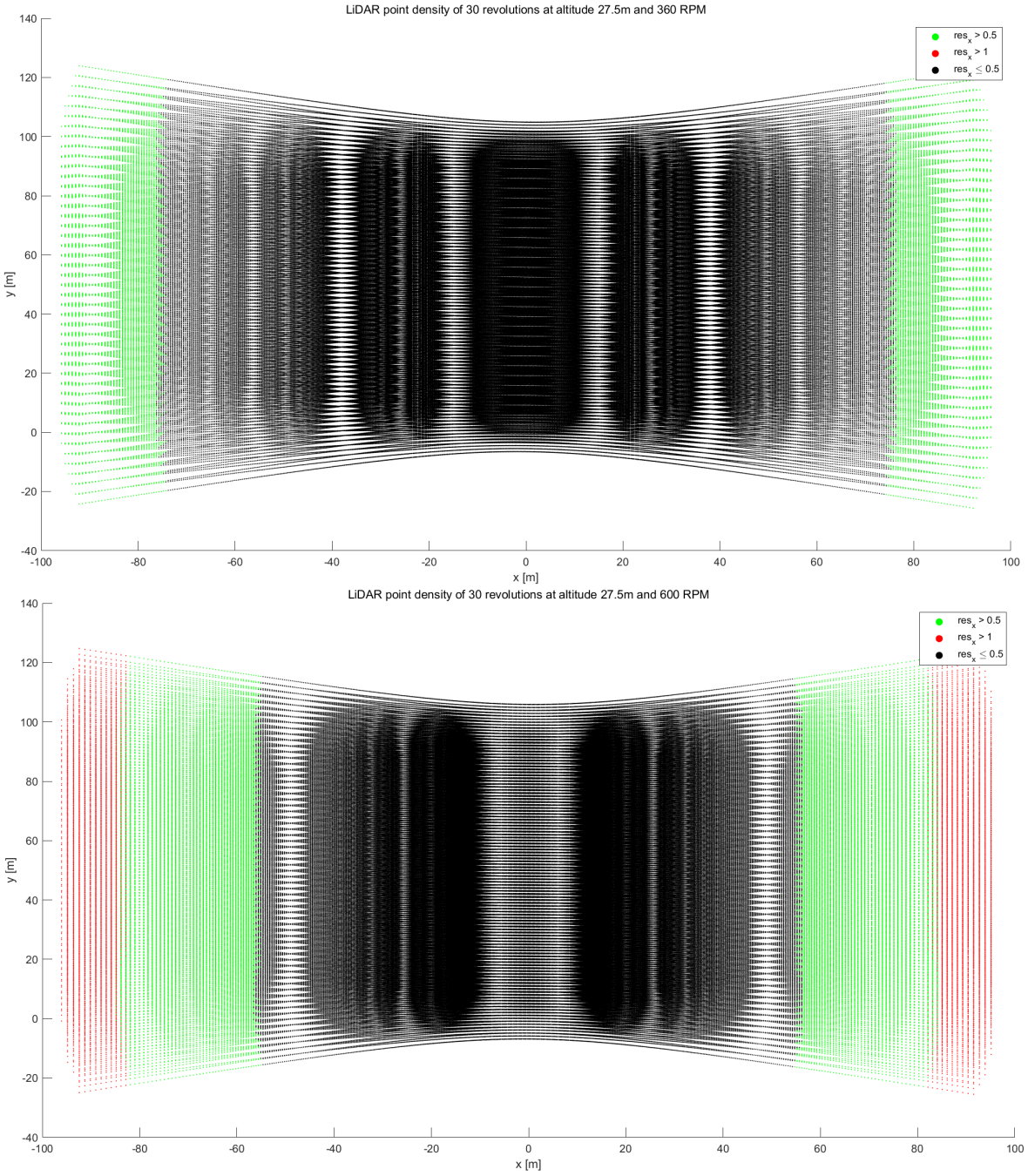

Figure 6.10: As Figure 6.9, but for 30 revolutions.

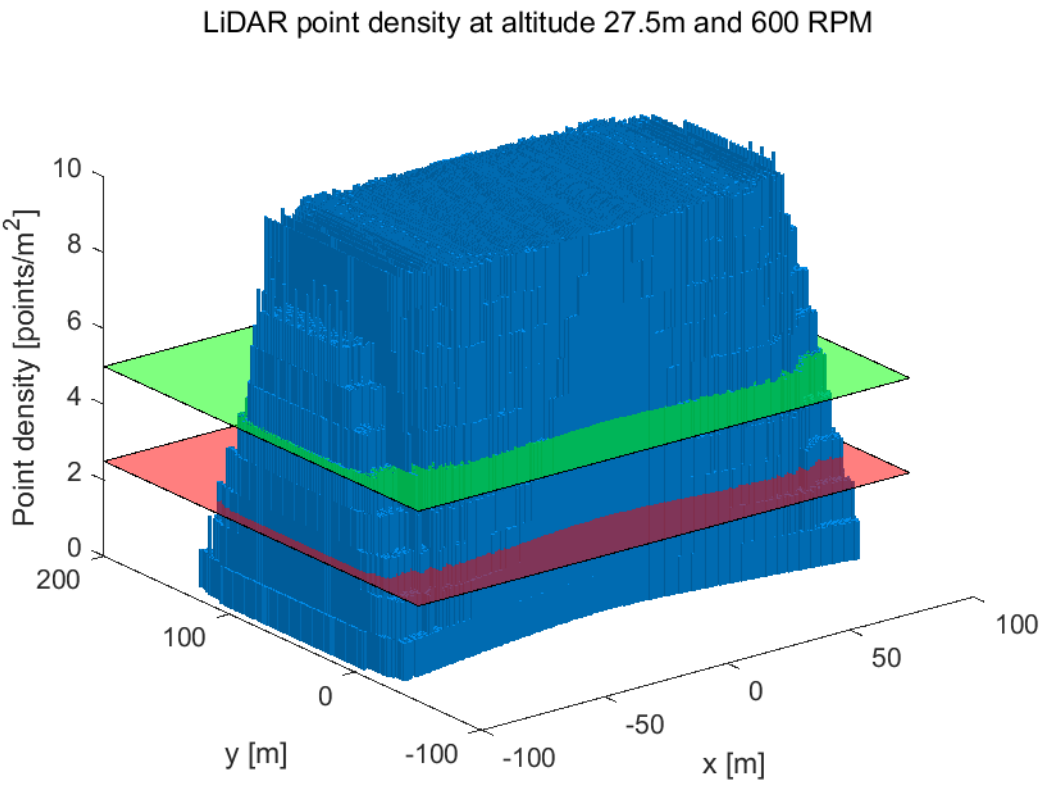

Figure 6.11: Histogram of the point density for 10 Hz rotation rate.

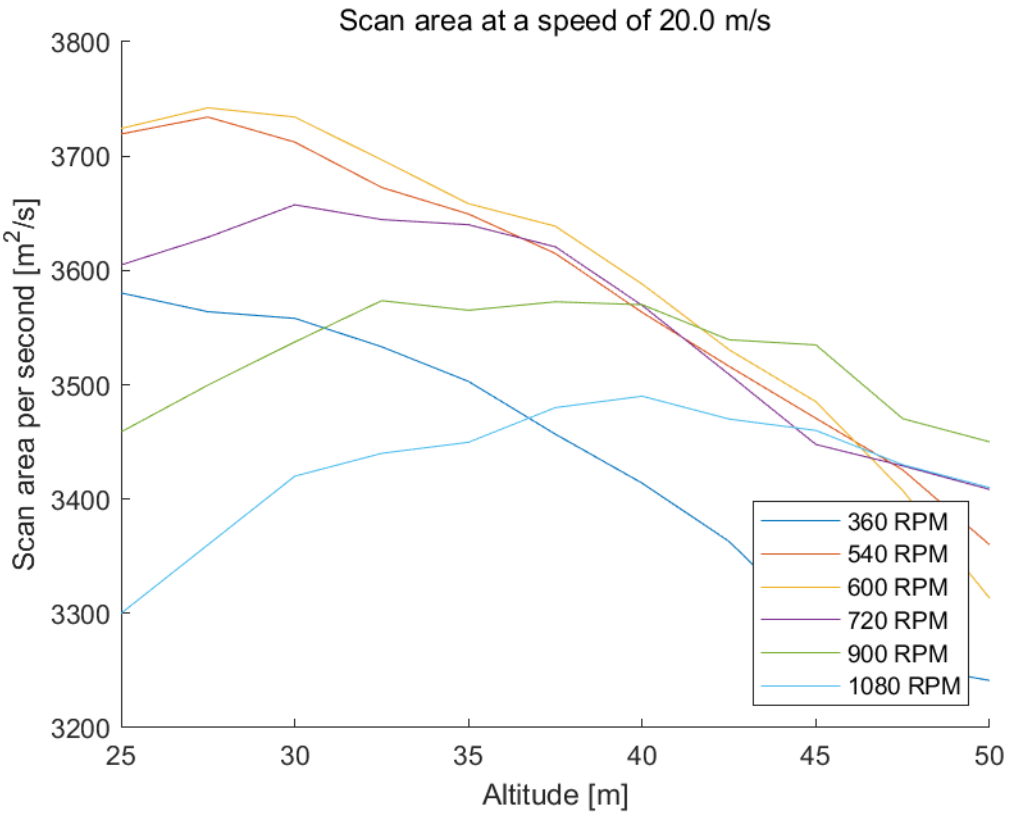

Figure 6.12: The area coverage of the LiDAR system for different altitudes and rotation rates. A high rotation rate has a smaller horizontal range due to a lower horizontal resolution, but has a higher vertical resolution, thus allowing for higher speeds. A low altitude creates a highly peaked distribution in the point density, with very high density right under the drone and low density further away. On the other hand, a high altitude will have a smaller horizontal range since this is limited by the total LiDAR range of 100 m. Hence there is an optimum in the LiDAR rotation speed and altitude. For a flight speed of 20 $\mathrm{m\,s^{-1}}$, the optimal configuration is an altitude of 27.5 m and a rotation rate of 10 Hz or 600 RPM.

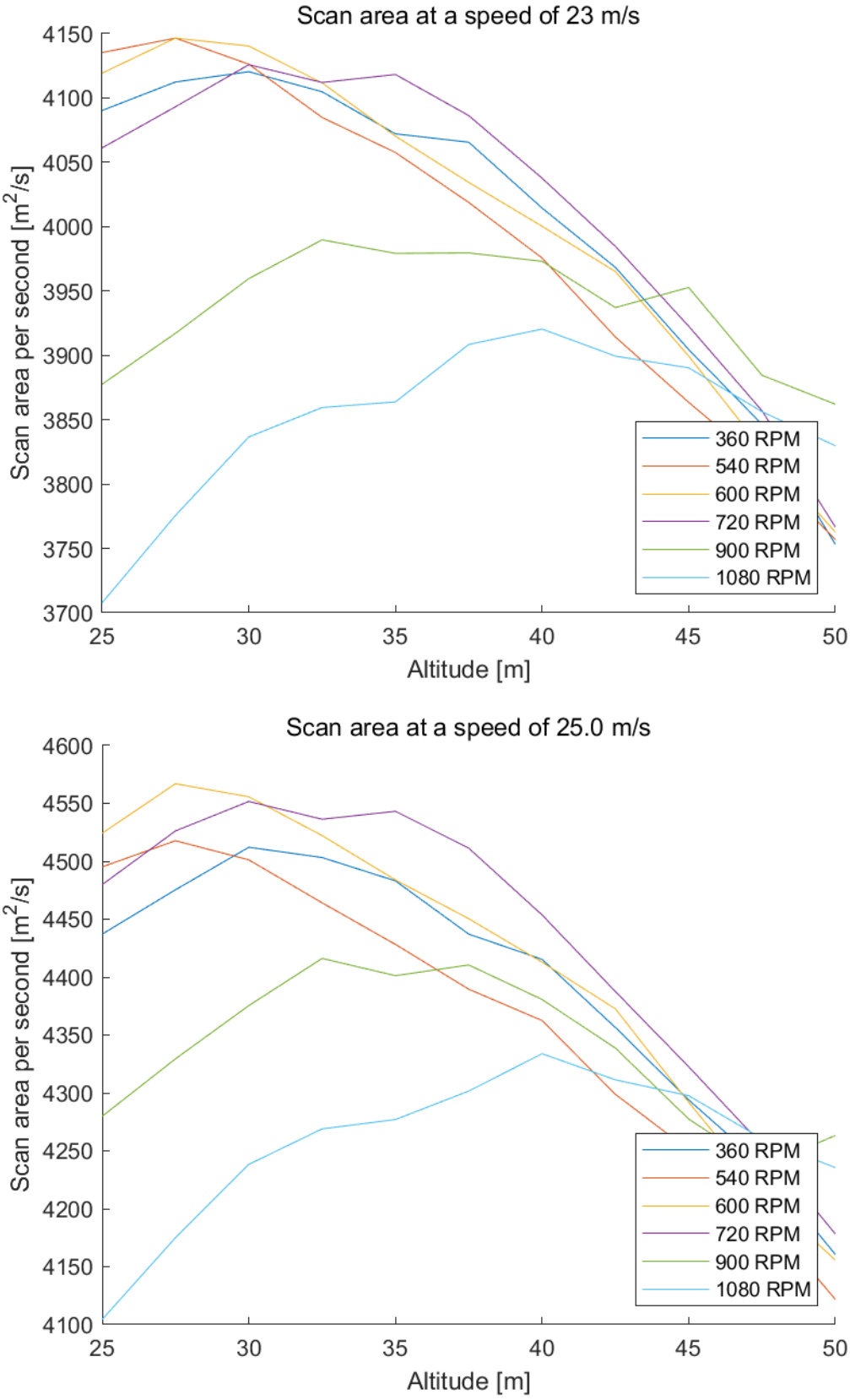

Figure 6.13: Figure 6.12, but for 23 $\mathrm{m\,s^{-1}}$ and 25 $\mathrm{m\,s^{-1}}$. The same calculations went into these plot as those for Figure 6.12. As expected, the area coverage increases linearly with flight speed. 600 RPM remains the optimal rotations rates at these higher speeds.

7

System integration

7.1. Introduction

In the previous chapters, the fuel cell, the drone, and the LiDAR system were discussed. Now we'll put them all together and finalize the design.

7.2. Weight and Power

One of the most important parameters of aerial vehicles is weight. Any increase in the designed weight of an aircraft will necessitate a larger engine, fuel tank, wing and body, etc., which further adds to the weight.

At the end of Chapter 4, it was mentioned that according to empirical values of the power consumption, the fuel tank does not contain enough hydrogen to fly more than 50 km. This is far from the objective of tripling the current 60 km range of the Delftacopter. The most straightforward way to increase the range is to add more fuel tanks, which will of course increase the total weight of the system.

Table 7.1 gives the total weight of the drone with one fuel tank. Adding another fuel tank increases the weight by 550 g, but will be very beneficial for the range. Figure 7.1 shows the power consumption and flight time for 1–6 fuel tanks. Note that they were calculated by scaling the theoretical power consumption as in Figure 4.11. The efficiency factors used to calculate the flight time are stated in Section 4.4.3. For 6 fuel tanks, the fuel cell cannot deliver enough (nominal) power at any flight speed, and is thus unfeasible. The extra weight has an adverse effect on the flight performance via the drag polar. Larger weight requires higher lift and drag coefficient. The necessary lift coefficient can be calculated from the balance between lift and weight which is maintained during cruise:

$$L = 0.9 C_L \rho S V^2 \tag{7.1}$$

$$L = W \Rightarrow C_L = \frac{W}{0.9 \rho S V^2} \tag{7.2}$$

Component	Weight [g]
Fuel cell	810
System components	250
Fuel tank (1x)	450
System components	100
Battery	250
LiDAR	590
System components	200
Delftacopter	2200
Total	4900

Table 7.1: Weights of all components. The fuel tank weight is for one tank. The Delftacopter weight is total weight of the current Delftacopter design without the batteries and payload. The "System components" for the fuel tank is an extra weight margin to include mounting.

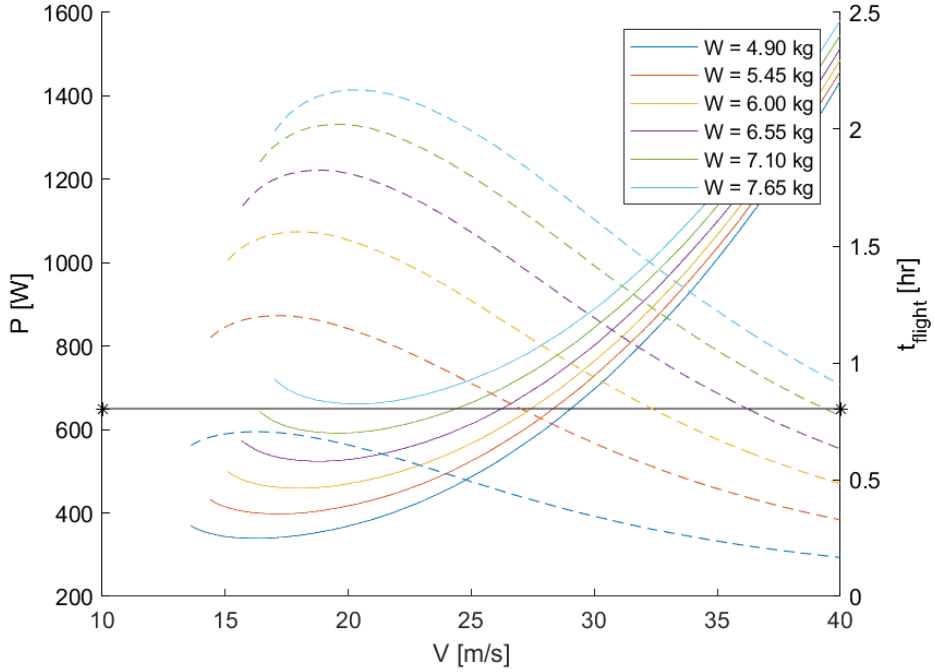

Figure 7.1: Flight speed versus power consumption (solid line) and flight time (dashed line) for one to six fuel tanks. The black line is nominal fuel cell power output. The gains per additional fuel tank goes down since the weight goes up, which then requires a higher lift and drag coefficient. Flight times can be further extended by replacing three small fuel tanks by the larger fuel tank that is manufactured by the same company. An estimated increase of 30% can be achieved. The design with 6 fuel tanks is not feasible as flying the drone will require more power than the fuel cell can deliver nominally. **See Chapter 8 for updated graph.**

where ρ is the atmosphere density in kg/m^3, S the area of a single wing. See Section 4.4.1 for an explanation for the modified lift formula. The atmosphere density at sea level of 1.225 kg/m^3 was used in the calculations. The higher C_L required for larger W corresponds to a higher C_D according to Figure 4.6, thus leading to higher power consumption. This has a negative effect on the flight time and range, the latter of which is shown in Figure 7.2. Nevertheless, adding extra fuel tanks significantly extend the range.

It should be noted that the weight of three small fuel tanks is 1350 g, and equals the weight of another fuel tank by the same company, the HDRX-030. This larger fuel tank however can store a volume of 3 L at 300 bar. The smaller fuel tanks can store 0.5 L at 500 bar, which contains the same amount of hydrogen as 0.75 L at 300 bar. The amount of hydrogen in the 3 L, 300 bar fuel tank is therefore 33% larger than for the three smaller fuel tanks combined. The range could therefore be extended by an additional 33% when replacing three fuel tanks for one, which amounts to 38 km. This replacement is important as it will also reduce the total volume of the fuel tanks, leading to a smaller fuselage and thus drag.

An interesting feature in the two figures is that for a heavier weight, maximal flight time shifts to higher speeds. Since flight time and distance are directly proportional, the maximal distance also moves to higher cruise speeds. These distance-maximizing speeds are achievable as they require less than the nominal power output of the fuel cell. However, the engine of the Delftacopter will have to be replaced as they exceed 22 m s^{-1}, see also Section 4.3. This will lead to a slightly larger weight for the 'Delftacopter' component in Table 7.1. As a reminder, the current engine weight is 385 g.

The final weight of this design is 7.1 kg, with the fuel cell system weighing 4.1 kg, which includes 2.25 kg of fuel tanks. This is far beyond the maximum takeoff weight of 4.5 kg of the original Delftacopter. In the next chapter, a configuration with 4 fuel tanks is considered with more accurate drag estimates.

7.3. Volume

The significantly higher weight of the vehicle is not the only problem. The sizes of the fuel cell and LiDAR systems (Table 7.2) are relatively large compared to the fuselage of about 100 mm by 200 mm. These components will therefore lead to additional air drag, see Chapter 8.

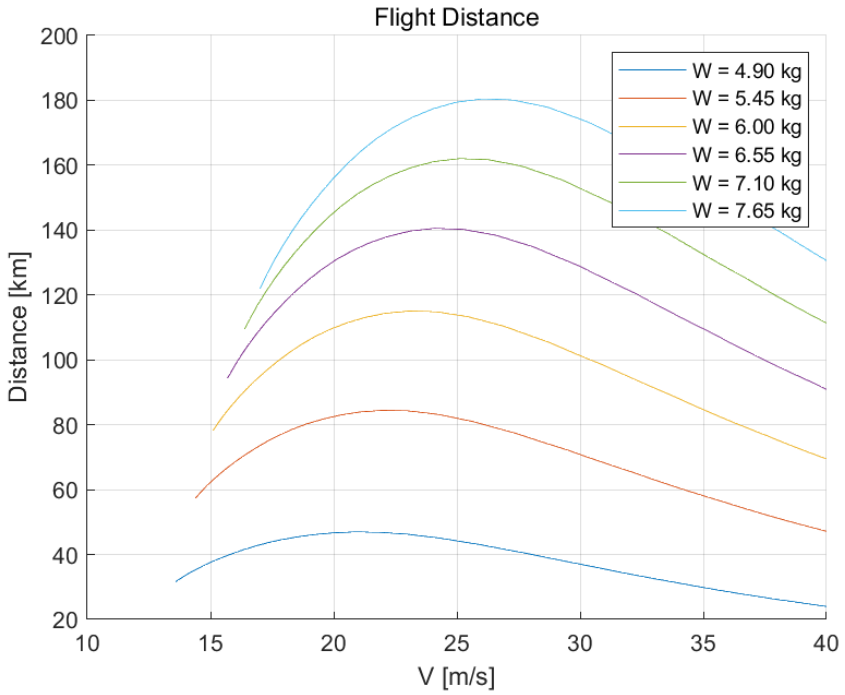

Figure 7.2: Flight distance achieved for one to six fuel tanks. **See Chapter 8 for updated graph.**

Component	dimensions
0.5 L fuel tank	diameter: 80 mm, length: 190 mm
3 L fuel tank	diameter: 116 mm, length: 444 mm
fuel cell	196 × 88 × 140 mm
emergency battery	140 × 30 × 20 mm
LiDAR sensor	diameter: 103.3 mm, length: 71.7 mm

Table 7.2: Size parameters of the fuel cell and LiDAR systems.

fuel tanks	area covered [km^2]
1	8.73
2	15.43
3	20.54
4	24.38
5	27.18
6	29.19

Table 7.3: **More accurate values are given in Chapter 8**. Area covered per flight by the LiDAR drone flying at 20 m s^{-1}. Increasing the flight speed is beneficial for the range of the drone, and therefore also the area coverage.

7.4. Area Coverage and Flight Capabilities

The area covered by the LiDAR system is displayed in Table 7.3 for 1 to 6 fuel tanks. These values are based on the flight speed of 20 m s^{-1}, which corresponds to area coverage of 3740 m^2/s. Flying at 23 m s^{-1} and 25 m s^{-1} give area coverage of 4240 m^2/s, and 4567 m^2/s. As was shown in Figure 8.4, increasing the flight speed will increase the area covered per second. Figures 7.2 and 8.4 also show that the range is increased at higher speed for larger numbers of fuel tanks. For these reasons, it is beneficial to fly at higher speeds.

The second column in Table 5.1 includes the sizes of the study area, which range from small forests of several square kilometers to larger geographical regions of hundreds of square kilometers, up to entire provinces or small nations of tens of thousands of square kilometers. The drone as designed in this thesis should be able to cover the larger geographical regions within the time span of a week.

7.5. Comparison of result

Analysis of fuel cell aerial vehicles was recently carried out in a MSc thesis by fellow student Yash Tambi.[1] The resulting model calculates the mass of the fuel cell system for an arbitrary flight mission profile, based on certain component weights and capacities. Its output is shown in Table 7.4.

Comparing this with Section 7.2, the model suggests a lighter system is possible. The mass difference is a significant 0.6 kg. The discrepancy comes mostly from the difference in BOP, which is twice as small in the model compared to those seen in Table 7.1. In addition, the battery is lighter, which is not surprising since the battery in the design of this thesis can deliver 650 W for 2 min, which is more than necessary for the flight mission.

Apart from that, the model seems to agree surprisingly well with our findings. Notably, the fuel cell and fuel tank weights are practically identical despite our methods being unrelated.

[1] His thesis can be accessed on `http://resolver.tudelft.nl/uuid:4ed8460c-d33c-44c3-a31e-e2bebc7df8d4`. Note however that it is under a five year embargo until May 2024

INPUT	
FC Power Density	802 $W kg^{-1}$
FC Nominal Efficiency	0.5
Fuel Utilization	0.94
FC BOP Weight Factor	0.236
Fuel Energy Density	32 790 $Wh kg^{-1}$
Fuel Tank Storage Density	0.042 kgH_2/kg
Battery Power Density	3250 $W kg^{-1}$
Battery Energy Density	108.3 $Wh kg^{-1}$
Battery BOP Weight Factor	0.15
FLIGHT MISSION	
Hover/climb power	1.2 kW
climb time	1 min
Hover/descent power	1 kW
descent time	1 min
Cruise power kW	0.65 kW
Cruise time	145.8 min
OPTIMIZATION	
Exit flag	2
Iterations	8771
FUEL CELL (exc. BOP)	
FC weight	0.81 kg
Nominal power	0.65 kW (climb)
	0.50 kW (descent)
	0.65 kW (cruise)
Fuel weight	0.094 kg
Tank weight	2.25 kg
BOP weight	0.19 kg
BATTERY (cell only)	
Weight	0.17 kg
Power	0.55 kW (climb)
	0.50 kW (descent)
	0 kW (cruise)
BOP weight	0.026 kW
Energy	0.019 kWh
OVERALL	
Total usable energy	1.57 kWh
Total weight	3.54 kg

Table 7.4: Results from a model by a fellow student, Yash Tambi. Output values for the fuel cell and battery are without the BOP. The overall values include BOP Weight, but exclude BOP Power. The weight of this fuel cell system is significantly lighter.

8

Improved drag estimation

Previously, the effects of adding the extra components on the aerodynamics has not been taken into account. In this appendix, a simple 3D model is made of the fuselage with the additional components, so that the increased drag can be roughly estimated.

8.1. Configuration of components

Due to the size of the components and the limited volume behind the fuselage, it is not possible to attach the entire fuel cell and LiDAR systems in that area. In particular, there is not enough space for the 3 L fuel tank, which would thus have to be mounted on one of the sides of the fuselage. However, this would cause a shift the center of gravity which has to be compensated for. A simple solution is to use only the 0.5 L fuel tanks. By using four of these fuel tanks, it's easy to find a symmetric configuration.

The goal is to find the configuration with the lowest drag. This is achieved when components are located behind one another, thus decreasing frontal surface area. The configuration is shown in Figure 8.1. When the Delftacopter is resting, there is around 200 mm between the back of the fuselage and the ground. This is more or less the length of the fuselage itself. With around 200 mm in height, i.e. between the two wings, there is almost enough space to fit the fuel cell and LiDAR sensor on top of each other. In this configuration, the LiDAR sensor is slightly protruding under the lower wing by about 25 mm, taking into account the airfoil thickness of 18.2 mm. This should not cause a significant drag increase. On the other hand, the fuel tanks almost double the frontal surface which will double the drag caused by the body.

8.2. Double body drag

Drag caused by increasing model complexity of the drone are shown in Figure 8.2. The drag contribution from the body was calculated as the difference between "XFLR5 wing" and "body". This was then multiplied by two and added along with the similarly calculated drag contribution from the extra parts. This is the drag polar of our configuration from the previous Section.

The higher drag will lead to a higher power consumption via $P = VD$. The power consumption was once again calculated via scaling, and the scaling factor used now is the factor between the "body" drag coefficients and "2x body" drag coefficients.

The results, Figure 8.3, indicate that the configuration with 5 fuel tanks is not feasible anymore. Therefore the new 4 fuel tank configuration as was shown in Figure 8.1 is a better optimal, as it allows for a larger range of speeds.

The removal of one fuel tank along with the more realistic drag estimates has reduced maximal flight distance to 116.4 km (Figure 8.4) which is covered in 1.38 h at a speed of around 22.5 $\mathrm{m\,s^{-1}}$. Total area covered per flight would be 21.78 $\mathrm{km^2}$. Total mass has been reduced to 6.55 kg.

8.3. MTOW bottleneck

The current Delftacopter design has a maximum takeoff weight of 4.5 kg. The limiting factor is the combination of the engine and propeller. Upgrading the engine, which has a mass of 385 g, should not lead to a noticeable increase in weight. The propeller needs to be upgraded as well. From Figure 8 in [16], one can

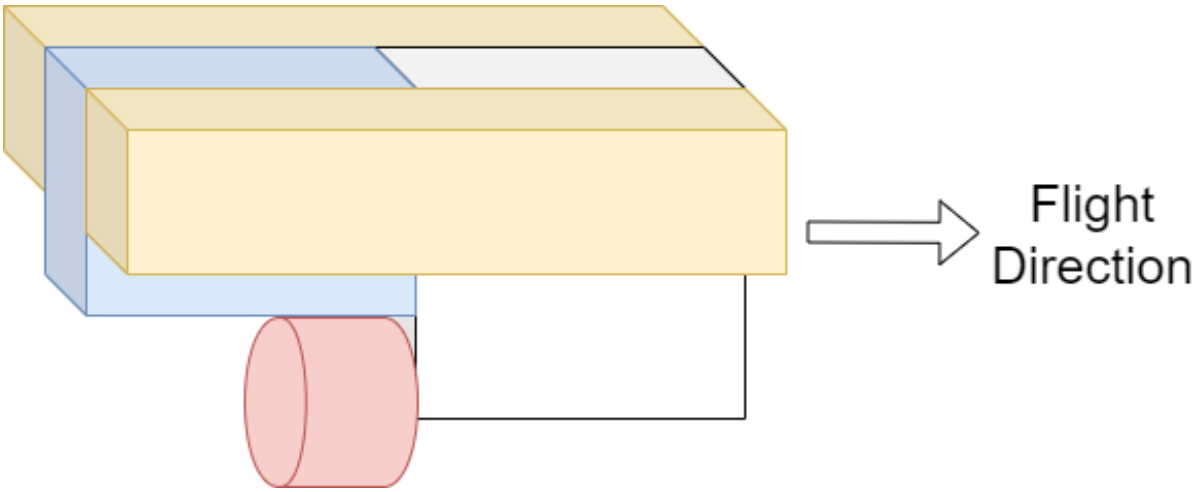

Figure 8.1: A drawing of the configuration for the four cylindrical fuel tanks (orange, two on either side), the fuel cell (blue) and the LiDAR sensor (red), attached to the fuselage (white). The propeller is on the right side.

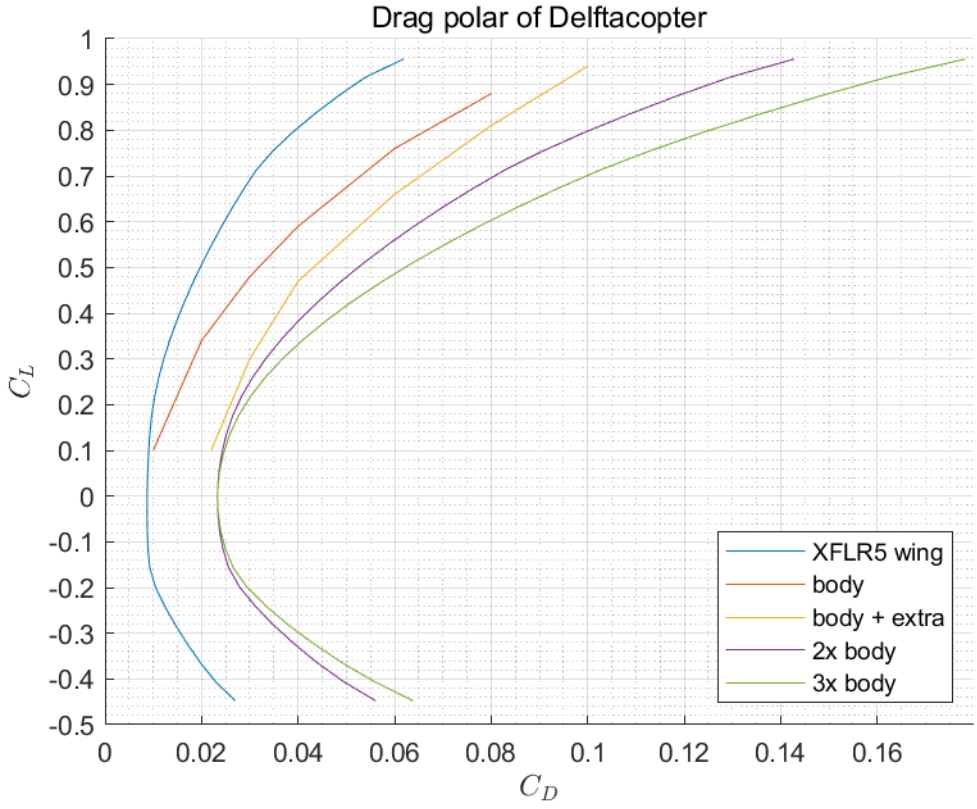

Figure 8.2: Drag polar contributions taken directly from [16], except for the "2x body" and "3x body" curve. The model for "XFLR5 wing" consists of only the wings, leaving out the body or extra parts. "2x body" consists of everything with doubled contributions by the "body".

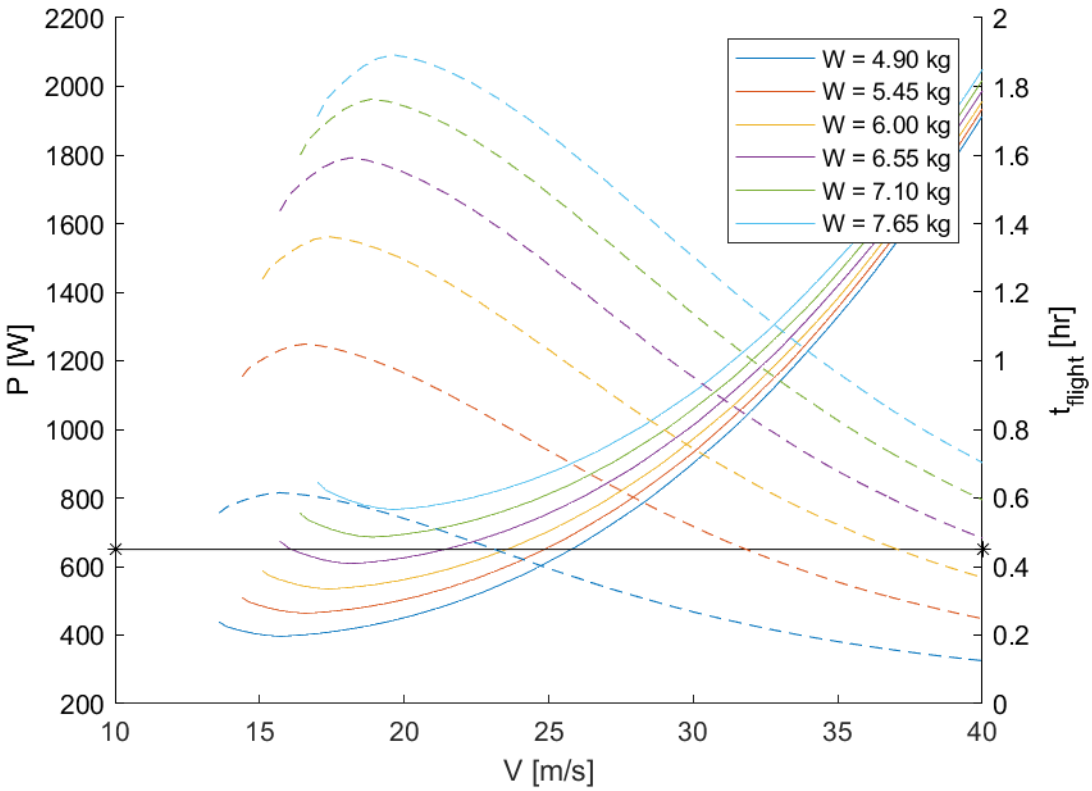

Figure 8.3: (Same as Figure 7.1.) Power consumption with twice the fuselage frontal area coming from the hydrogen fuel tanks. Compared to the previous estimate, the 5 fuel tank configuration has become unrealistic.

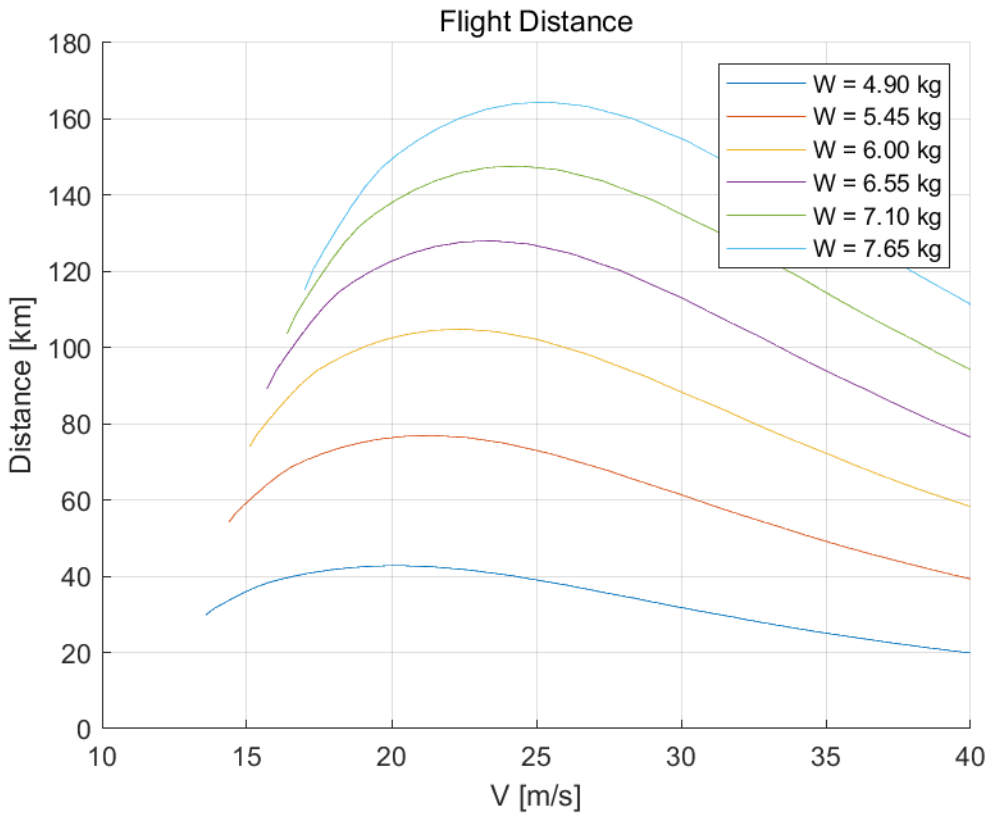

Figure 8.4: Distance reached at constant speed before fuel tanks are empty.

fuel tanks	area covered [km^2]
1	7.27
2	12.99
3	17.44
4	20.87
5	23.48
6	25.41

Table 8.1: Area covered per flight at 20 m s^{-1} for different amounts of on board fuel tanks. The power output of the fuel cell limits the maximum amount of fuel tanks to 4. At 4 fuel tanks, raising the speed from 20 to 22.5 m s^{-1} can increase the area from 20.87 to 21.78 km^2.

see that the propeller cannot deliver 650 W. However, the propeller also does not contribute significantly to the overall weight. In conclusion, this bottleneck can be overcome without further modifications to the structure.

9

General Conclusion

We have set out to modify the Delftacopter, powered by batteries, to a design powered by a hydrogen fuel cell, capable of flying at least 180 km, and of scanning forest tree heights with at least 5 points per square meter for soil organic carbon measurements.

9.1. Results

The commercial fuel cell by Intelligent Energy, which can deliver 650 W, along with the 0.5 L 500 bar (HDRX-005-500) hydrogen fuel tank by MEYER, were selected for their light weight and performance. The fuel cell can deliver more power than the original design, but this extra power has been necessary to carry the fuel tanks in order to surpass the original range of the drone. The LiDAR sensor is the Puck LITE by Velodyne and was selected for its high pulse frequency, sufficient range and low weight.

Considering that the weight has increased by around %60, the Delftacopter would have to be redesigned in order to accommodate the changes, since it cannot fly at the optimal lift to drag ratio and has surpassed its maximal takeoff weight of 4.5 kg. The volume of the added components are quite significant relative to the original Delftacopter fuselage. When taking into account additional drag due to protrusions, the feasible configuration is one with 4 small fuel tanks. The weight in this case has been reduced to 6.55 kg.

With this configuration, a flight distance of 116 km can be achieved at 22.5 $\mathrm{m\,s^{-1}}$, covering 23 $\mathrm{km^2}$ per flight of 1.5 h.

9.2. Further Research

- Not much analysis was performed for the fuel cell. Some thermodynamic analysis may be useful, as fuel cells produce substantial amounts of heat. In order to perform such an analysis, it may be necessary to have a model of the positioning of all components, including the fuel cell, fuel tank(s) and LiDAR sensor.
- The range of the LiDAR system is stated as 100 m by the manufacturer. However, this may only be achieved under ideal conditions. Further analysis or field testing is required to determine its practical range under various conditions.
- In the configuration described in Chapter 8, the larger fuel tanks (3 L 300 bar (HDRX-030)) were not used due to the 650 W power output limit. By implementing a more powerful fuel cell, along with a suitable engine and propeller, the 4 small 80 mm diameter fuel tanks could be replaced by 2 large 116 mm tanks, with minimal additional drag. The two large fuel tanks can store twice the hydrogen of 4 small fuel tanks, thus range could be nearly doubled.

Bibliography

[1] C. Hug A, A. Ullrich B, and A. Grimm C. Litemapper-5600 – a waveform-digitizing lidar terrain and vegetation mapping system.

[2] Kabindra Adhikari, Alfred E. Hartemink, Budiman Minasny, Rania Bou Kheir, Mette B. Greve, and Mogens H. Greve. Digital mapping of soil organic carbon contents and stocks in denmark. *PLOS ONE*, 9(8): 1–13, 08 2014. doi: 10.1371/journal.pone.0105519. URL https://doi.org/10.1371/journal.pone.0105519.

[3] G. Aka, E. Reino, D. Vivien, F. Balembois, P. Georges, and B. Ferrand. Laser emission of nd:asl at 900 nm. In *Advanced Solid-State Lasers*, page TuC5. Optical Society of America, 2002. doi: 10.1364/ASSL.2002.TuC5. URL http://www.osapublishing.org/abstract.cfm?URI=ASSL-2002-TuC5.

[4] Hans-Erik Andersen, Stephen E. Reutebuch, and Robert J. McGaughey. A rigorous assessment of tree height measurements obtained using airborne lidar and conventional field methods. *Canadian Journal of Remote Sensing.*, 32(5):355–366, 2006.

[5] A.J. Appleby. From sir william grove to today: fuel cells and the future. *Journal of Power Sources*, 29 (1):3 – 11, 1990. ISSN 0378-7753. doi: https://doi.org/10.1016/0378-7753(90)80002-U. URL http://www.sciencedirect.com/science/article/pii/037877539080002U. Proceedings of the Grove Anniversary Fuel Cell Symposium.

[6] E.P Baltsavias. Airborne laser scanning: basic relations and formulas. *ISPRS Journal of Photogrammetry and Remote Sensing*, 54(2):199 – 214, 1999. ISSN 0924-2716. doi: https://doi.org/10.1016/S0924-2716(99)00015-5. URL http://www.sciencedirect.com/science/article/pii/S0924271699000155.

[7] F. Barbir and T. Gómez. Efficiency and economics of proton exchange membrane (pem) fuel cells. *International Journal of Hydrogen Energy*, 22(10):1027 – 1037, 1997. ISSN 0360-3199. doi: https://doi.org/10.1016/S0360-3199(96)00175-9. URL http://www.sciencedirect.com/science/article/pii/S0360319996001759.

[8] Edward Barnes, Kenneth Sudduth, John W. Hummel, Scott Lesch, Dennis Corwin, Chenghai Yang, Craig Daughtry, and Walter C. Bausch. Remote and ground-based sensor techniques to map soil properties. *Photogrammetric Engineering & Remote Sensing*, 69, 06 2003. doi: 10.14358/PERS.69.6.619.

[9] N.H. Batjes. Total carbon and nitrogen in the soils of the world. *European Journal of Soil Science*, 65: 10–21, 2014. doi: 10.1111/ejss.12114_2.

[10] Amado Alberto Lopez Bautista. Biomass carbon estimation and mapping in the subtropical forest of chitwan, nepal: A comparison between vhr geo-eye satellite images and airborne lidar data. 2012.

[11] E. Ben-Dor, R.G. Taylor, J. Hill, J.A.M. Demattê, M.L. Whiting, S. Chabrillat, and S. Sommer. Imaging spectrometry for soil applications. volume 97 of *Advances in Agronomy*, pages 321 – 392. Academic Press, 2008. doi: https://doi.org/10.1016/S0065-2113(07)00008-9. URL http://www.sciencedirect.com/science/article/pii/S0065211307000089.

[12] Gouri Sankar Bhunia, Pravat Kumar Shit, and Hamid Reza Pourghasemi. Soil organic carbon mapping using remote sensing techniques and multivariate regression model. *Geocarto International*, 0(0):1–12, 2017. doi: 10.1080/10106049.2017.1381179.

[13] Barry A. Bodhaine, Norman B. Wood, Ellsworth G. Dutton, and James R. Slusser. On rayleigh optical depth calculations. *Journal of Atmospheric and Oceanic Technology*, 16(11):1854–1861, 1999. doi: 10.1175/1520-0426(1999)016<1854:ORODC>2.0.CO;2. URL https://doi.org/10.1175/1520-0426(1999)016<1854:ORODC>2.0.CO;2.

[14] P. A. Budni, L. A. Pomeranz, M. L. Lemons, C. A. Miller, J. R. Mosto, and E. P. Chicklis. Efficient mid-infrared laser using 1.9-µm-pumped ho:yag and zngep2 optical parametric oscillators. *J. Opt. Soc. Am. B*, 17(5):723–728, May 2000. doi: 10.1364/JOSAB.17.000723. URL http://josab.osa.org/abstract.cfm?URI=josab-17-5-723.

[15] Josep G Canadell, Diane E Pataki, Roger Gifford, Richard A Houghton, Yiqi Luo, Michael R Raupach, Pete Smith, and Will Steffen. Saturation of the terrestrial carbon sink. In *Terrestrial ecosystems in a changing world*, pages 59–78. Springer, 2007.

[16] Christophe De Wagter, Rick Ruijsink, Ewoud J. J. Smeur, Kevin G. van Hecke, Freek van Tienen, Erik van der Horst, and Bart D. W. Remes. Design, control, and visual navigation of the delftacopter vtol tail-sitter uav. *Journal of Field Robotics*, 0(0). doi: 10.1002/rob.21789. URL https://onlinelibrary.wiley.com/doi/abs/10.1002/rob.21789.

[17] Mark Drela. Xfoil: An analysis and design system for low reynolds number airfoils. In *Low Reynolds number aerodynamics*, pages 1–12. Springer, 1989.

[18] Food and Agriculture Organization of the United Nations. Soil organic carbon: the hidden potential, 2017. URL http://www.fao.org/3/a-i6937e.pdf%20.

[19] Cécile Gomez, Raphael A. Viscarra Rossel, and Alex B. McBratney. Soil organic carbon prediction by hyperspectral remote sensing and field vis-nir spectroscopy: An australian case study. *Geoderma*, 146: 403–411, 2008. doi: 10.1016/j.geoderma.2008.06.01.

[20] I.E. Gordon, L.S. Rothman, C. Hill, R.V. Kochanov, Y. Tan, P.F. Bernath, M. Birk, V. Boudon, A. Campargue, K.V. Chance, B.J. Drouin, J.-M. Flaud, R.R. Gamache, J.T. Hodges, D. Jacquemart, V.I. Perevalov, A. Perrin, K.P. Shine, M.-A.H. Smith, J. Tennyson, G.C. Toon, H. Tran, V.G. Tyuterev, A. Barbe, A.G. Császár, V.M. Devi, T. Furtenbacher, J.J. Harrison, J.-M. Hartmann, A. Jolly, T.J. Johnson, T. Karman, I. Kleiner, A.A. Kyuberis, J. Loos, O.M. Lyulin, S.T. Massie, S.N. Mikhailenko, N. Moazzen-Ahmadi, H.S.P. Müller, O.V. Naumenko, A.V. Nikitin, O.L. Polyansky, M. Rey, M. Rotger, S.W. Sharpe, K. Sung, E. Starikova, S.A. Tashkun, J. Vander Auwera, G. Wagner, J. Wilzewski, P. Wcisło, S. Yu, and E.J. Zak. The hitran2016 molecular spectroscopic database. *Journal of Quantitative Spectroscopy and Radiative Transfer*, 203:3 – 69, 2017. ISSN 0022-4073. doi: https://doi.org/10.1016/j.jqsrt.2017.06.038. URL http://www.sciencedirect.com/science/article/pii/S0022407317301073. HITRAN2016 Special Issue.

[21] Wang Huan-Xue, Liu Jian-Guo, and Zhang Tian-Shu. Estimation of random errors for lidar based on noise scale factor. *Chinese Physics B*, 24(8):084213, 2015. URL http://stacks.iop.org/1674-1056/24/i=8/a=084213.

[22] Janna Huuskonen and Timo Oksanen. Soil sampling with drones and augmented reality in precision agriculture. *Computers and Electronics in Agriculture*, 154:25 – 35, 2018. ISSN 0168-1699. doi: https://doi.org/10.1016/j.compag.2018.08.039. URL http://www.sciencedirect.com/science/article/pii/S0168169918301650.

[23] IPCC, V. Masson-Delmotte, P. Zhai, H. O. Pörtner, D. Roberts, J. Skea, P.R. Shukla, A. Pirani, W. Moufouma-Okia, R. Pidcock C. Péan, S. Connors, J. B. R. Matthews, X. Zhou Y. Chen, M. I. Gomis, E. Lonnoy, T. Maycock, T. Waterfield (eds.) M. Tignor, and Switzerland World Meteorological Organization, Geneva. Summary for Policymakers. In: Global warming of 1.5°C. An IPCC Special Report on the impacts of global warming of 1.5°C above pre-industrial levels and related global greenhouse gas emission pathways, in the context of strengthening the global response to the threat of climate change, sustainable development, and efforts to eradicate poverty. page 32, 2018.

[24] Jānis Ivanovs and Andis Lazdins. Engineering for rural development evaluation of tree height and number of trees using lidar data. 05 2018. doi: 10.22616/ERDev2018.17.N153.

[25] Donggeun Kim, Younghwan Son, Jaesung Park, Taejin Kim, and Jihun Jeon. Evaluation of calibration method for field application of uav-based soil water content prediction equation. *Advances in Civil Engineering*, 2019. doi: https://doi.org/10.1155/2019/2486216.

[26] C. Klingenfuß, N. Roßkopf, J. Walter, C. Heller, and J. Zeitz. Soil organic matter to soil organic carbon ratios of peatland soil substrates. *Geoderma*, 235-236:410 – 417, 2014. ISSN 0016-7061. doi: https://doi.org/10.1016/j.geoderma.2014.07.010. URL http://www.sciencedirect.com/science/article/pii/S001670611400281X.

[27] Gopal Krishan, s Saha, Suresh Kumar, and Patel R. *Remote Sensing in Soil Fertility Evaluation and Management*, pages 509–533. 01 2014.

[28] R. Lal. Soil carbon sequestration impacts on global climate change and food security. *Science*, 304: 1623–1627, 2004. doi: 10.1126/science.1097396.

[29] Rattan Lal. Soil health and carbon management. *Food and Energy Security*, 5(4):212–222, 2016. doi: 10.1002/fes3.96. URL https://onlinelibrary.wiley.com/doi/abs/10.1002/fes3.96.

[30] Rattan Lal, Pete Smith, Hermann F. Jungkunst, William J. Mitsch, Johannes Lehmann, P.K. Ramachandran Nair, Alex B. McBratney, João Carlos de Moraes Sá, Julia Schneider, Yuri L. Zinn, Alba L.A. Skorupa, Hai-Lin Zhang, Budiman Minasny, Cherukumalli Srinivasrao, and Nijavalli H. Ravindranath. The carbon sequestration potential of terrestrial ecosystems. *Journal of Soil and Water Conservation*, 73(6): 145A–152A, 2018. doi: 10.2489/jswc.73.6.145A. URL http://www.jswconline.org/content/73/6/145A.short.

[31] James Larminie and Andrew Dicks. *Fuel Cell Systems Explained*. John Wiley & Sons, 2003.

[32] Chao Li, Yanli Xu, Zhaogang Liu, Shengli Tao, Fengri Li, and Jingyun Fang. Estimation of forest topsoil properties using airborne lidar-derived intensity and topographic factors. *Remote Sensing*, 8(7), 2016. ISSN 2072-4292. doi: 10.3390/rs8070561. URL http://www.mdpi.com/2072-4292/8/7/561.

[33] J. Mariens, A. Elham, and M. J. L. van Tooren. Quasi-three-dimensional aerodynamic solver for multidisciplinary design optimization of lifting surfaces. *Journal of Aircraft*, 51(2):547–558, 2014. doi: 10.2514/1.C032261. URL https://doi.org/10.2514/1.C032261.

[34] Etsuo Morishita. Biplane aerodynamics revisited. 02 2016. doi: 10.14311/TPFM.2016.019.

[35] Katsuhisa Niwa, Jun Yokobori, Chiharu Hongo, and Osamu Nagata. Estimating soil carbon stocks in an upland area of tokachi district, hokkaido, japan, by satellite remote sensing. *Soil Science and Plant Nutrition*, 57(2):283–293, 2011. doi: 10.1080/00380768.2011.557769.

[36] Sebastian Oleire-Oltmanns, Irene Marzolff, Klaus Daniel Peter, and Johannes B. Ries. Unmanned aerial vehicle (uav) for monitoring soil erosion in morocco. *Remote Sensing*, 4(11):3390–3416, 2012. ISSN 2072-4292. doi: 10.3390/rs4113390. URL https://www.mdpi.com/2072-4292/4/11/3390.

[37] Eugenia Pérez and Pilar García. Monitoring soil erosion by raster images: From aerial photographs to drone taken pictures. *Eur. J. Geogr*, 8:116–128, 2017.

[38] S.M.M. Rasel, T.A. Groen, Y.A. Hussin, and I.J. Diti. Proxies for soil organic carbon derived from remote sensing. *International Journal of Applied Earth Observation and Geoinformation*, 59:157–166, 2017. doi: 10.1016/j.jag.2017.03.004.

[39] Alejandro Flores Reyes. Design and development of an uav with hybrid flight capabilities. Master's thesis, Centro de investigaciones en óptica, 8 2018.

[40] William F Ruddiman. The anthropogenic greenhouse era began thousands of years ago. *Climatic change*, 61(3):261–293, 2003.

[41] Calogero Schillaci, Marco Acutis, Luigi Lombardo, Aldo Lipani, Maria Fantappiè, Michael Märker, and Sergio Saia. Spatio-temporal topsoil organic carbon mapping of a semi-arid mediterranean region: The role of land use, soil texture, topographic indices and the influence of remote sensing data to modelling. *Science of the Total Environment*, 601–602:821–832, 2017. doi: 10.1016/j.scitotenv.2017.05.239.

[42] J.H. Seinfeld and S.N. Pandis. *Atmospheric chemistry and physics: from air pollution to climate change*. A Wiley interscience publication. Wiley, 1998. ISBN 9780471178156. URL https://books.google.nl/books?id=lK8PAQAAMAAJ.

[43] Omar Z. Sharaf and Mehmet F. Orhan. An overview of fuel cell technology: Fundamentals and applications. *Renewable and Sustainable Energy Reviews*, 32:810 – 853, 2014. ISSN 1364-0321. doi: https://doi.org/10.1016/j.rser.2014.01.012. URL http://www.sciencedirect.com/science/article/pii/S1364032114000227.

[44] J. Speight. *Lange's Handbook of Chemistry, 70th Anniversary Edition*. McGraw-Hill Standard Handbooks. McGraw-Hill Companies,Incorporated, 2004. ISBN 9780071432207. URL https://books.google.nl/books?id=p6MRAQAAMAAJ.

[45] Wei Su, Rui Liu, Ting Liu, Jianxi Huang, Xiaodong Zhang, and Junming Liu. The Estimation of Tree Height Based on LiDAR Data and QuickBird Imagery. In Daoliang Li and Yingyi Chen, editors, *6th Computer and Computing Technologies in Agriculture (CCTA)*, volume AICT-393 of *Computer and Computing Technologies in Agriculture VI*, pages 472–482, Zhangjiajie, China, October 2012. Springer. doi: 10.1007/978-3-642-36137-1_55. URL https://hal.inria.fr/hal-01348265.

[46] Bin Wang, Cathy Waters, Susan Orgill, Jonathan Gray, Annette Cowie, Anthony Clark, and De Li Liu. High resolution mapping of soil organic carbon stocks using remote sensing variables in the semi-arid rangelands of eastern australia. *Science of the Total Environment*, 630:367–378, 2018. doi: 10.1016/j.scitotenv.2018.02.204.

[47] S. Williamson, M. Lukic, and A. Emadi. Comprehensive drive train efficiency analysis of hybrid electric and fuel cell vehicles based on motor-controller efficiency modeling. *IEEE Transactions on Power Electronics*, 21(3):730–740, May 2006. ISSN 0885-8993. doi: 10.1109/TPEL.2006.872388.